SCIENCE CHINA
Earth Sciences

•RESEARCH PAPER•

September 2020 Vol.63 No.9: 1309–1329
https://doi.org/10.1007/s11430-019-9615-3

Elastic wave propagation and scattering in prestressed porous rocks

Li-Yun FU[1,2*], Bo-Ye FU[3,4,5], Weijia SUN[3], Tongcheng HAN[1,2] & Jianlin LIU[1,2]

[1] *Key Laboratory of Deep Oil and Gas, China University of Petroleum (East China), Qingdao 266580, China;*
[2] *Laboratory for Marine Mineral Resources, Qingdao National Laboratory for Marine Science and Technology, Qingdao 266071, China;*
[3] *Key Laboratory of Earth and Planetary Physics, Institute of Geology and Geophysics, Chinese Academy of Sciences, Beijing 100029, China;*
[4] *Institutions of Earth Science, Chinese Academy of Sciences, Beijing 100029, China;*
[5] *College of Earth and Planetary Sciences, University of Chinese Academy of Sciences, Beijing 100049, China*

Received August 16, 2019; revised April 8, 2020; accepted April 20, 2020; published online May 22, 2020

Abstract Poro-acoustoelastic theory has made a great progress in both theoretical and experimental aspects, but with no publications on the joint research from theoretical analyses, experimental measurements, and numerical validations. Several key issues challenge the joint research with comparisons of experimental and numerical results, such as digital imaging of heterogeneous poroelastic properties, estimation of acoustoelastic constants, numerical dispersion at high frequencies and strong heterogeneities, elastic nonlinearity due to compliant pores, and contamination by boundary reflections. Conventional poro-acoustoelastic theory, valid for the linear elastic deformation of rock grains and stiff pores, is modified by incorporating a dual-porosity model to account for elastic nonlinearity due to compliant pores subject to high-magnitude loading stresses. A modified finite-element method is employed to simulate the subtle effect of microstructures on wave propagation in prestressed digital cores. We measure the heterogeneity of samples by extracting the autocorrelation length of digital cores for a rough estimation of scattering intensity. We conductexperimental measurements with a fluid-saturated sandstone sample under a constant confining pressure of 65 MPa and increasing pore pressures from 5 to 60 MPa. Numerical simulations for ultrasound propagation in the prestressed fluid-saturated digital core of the sample are followed based on the proposed poro-acoustoelastic model with compliant pores. The results demonstrate a general agreement between experimental and numerical waveforms for different stresses, validating the performance of the presented modeling scheme. The excellent agreement between experimental and numerical coda quality factors demonstrates the applicability for the numerical investigation of the stress-associated scattering attenuation in prestressed porous rocks.

Keywords Poro-acoustoelasticity with compliant pores, Elastic waves, Prestressed porous rocks, Numerical modeling, Stress-induced scattering attenuation

Citation: Fu L, Fu B, Sun W, Han T, Liu J. 2020. Elastic wave propagation and scattering in prestressed porous rocks. Science China Earth Sciences, 63: 1309–1329, https://doi.org/10.1007/s11430-019-9615-3

1. Introduction

Acoustic velocities are sensitive to stresses in most porous rocks. Conventional descriptions of the stress-induced velocity variations in porous rocks are often based on microcrack models by assuming closure of microcracks or compression of grain contacts. As stressed by Winkler and McGowan (2004), a more general description that is model-independent by ignoring microstructures is based on the third-order nonlinear elasticity theory (i.e., poro-acoustoelastic theory). Because of great interesting to the knowledge of subsurface *in-situ* stresses in many application fields,

* Corresponding author (email: lfu@upc.edu.cn)

poro-acoustoelastic methods have the potential to monitor changes in the subsurface effective pressures and tectonic stresses. The poro-acoustoelastic response of porous rocks has been widely studied and well established, with most focusing on theoretical and experimental aspects (e.g., Johnson and Shankland, 1989; Meegan Jr. et al., 1993; Winkler and Liu, 1996). Theoretical solutions with effective elastic properties are only applicable to very simple media and cannot directly interpret laboratory measurements of real cores. Numerical methods with digital cores are perhaps an efficient alternative for general applicability, but to date, no publications are available on the numerical poro-acoustoelastic modeling. In this study, we attempt to develop a poro-acoustoelastic modeling scheme for ultrasonic wave propagation in prestressed, digital, and fluid-saturated heterogeneous rocks.

Stressed-induced scattering attenuation in ultrasonic wavelengths for prestressed fluid-saturated rocks is another major issue to motive the current study. With the extensive publications, scattering attenuation, caused by small-scale heterogeneities and commonly measured in the frequency range of 1–30 Hz, has been well established (Aki and Chouet, 1975). The resultant coda is a useful seismological tool to estimate the strength of heterogeneities in the lithosphere (Sato, 1977; Wu and Aki, 1985). On the other hand, scattering attenuation at high frequencies has long been interesting to geophysicists, because coda characteristics are more sensitive to small-scale microstructures in rocks. There have been some attempts to study scattering processes at high frequencies by physical modeling for dry rocks (Matsunami, 1991; Nishizawa et al., 1997; Sivaji et al., 2002; Fukushima et al., 2003). The resulting codas are used as an index to characterize rock heterogeneities because of the significant scattering effect occurring when wavelengths are comparable to the scale of pores and rock grains (Wu, 1989).

Few studies on coda attenuation in the ultrasonic frequency range are conducted for prestressed fluid-saturated rocks. Ultrasonic codas, as the tail portion of ultrasonic wavetrains in ultrasonic measurements, are important for such studies. Ultrasonic waves interact with microstructural heterogeneities on a scale of micrometers, where both the prestress and microstructural effects account for strong scattering attenuation at comparable wavelengths to the scale of pores and grains. However, in the past decades, ultrasonic codas from experimental measurements are often ignored as noises, possibly because of the size limitation of samples, the contamination of boundary reflections, the unknown heterogeneity in rocks, and the complexity of received waveforms (Stacey and Gladwin, 1981). As indicated by Toksöz et al. (1979), attenuation values are more difficult to obtain experimentally than velocities. Recent researches begin to address the scattering attenuation of experimental measurements from both the analytical solution (Galvin and Gurevich, 2007, 2009) and numerical modeling (Fu et al., 2014; Zhang et al., 2014) of Biot's poroelastic equations. An attempt to measure stress-induced ultrasonic scattering attenuation for prestressed fluid-saturated rocks has been made based on the single-scattering assumption (Guo and Fu, 2007; Guo et al., 2009) and the Monte Carlo simulation (Wei and Fu, 2014; Hu et al., 2018). The resulting conclusions from these studies, however, may be controversial because of the theoretical limitation of equations under prestressing conditions and the contaminated coda waves by boundary reflections from the side ends of a sample core. It is difficult to extract pure coda waves from ultrasonic measurements. With a controllable absorbing boundary, poro-acoustoelastic numerical simulations compared to experimental measurements for the same prestressed heterogeneous core can give important insights into the effect of core heterogeneities and experimental environments on ultrasonic coda waves.

One of the key issues to challenge the experimental and numerical comparison is the elastic nonlinearity due to compliant pores under large-magnitude stresses. It is probably the reason for the uncertain dependence of elastic moduli variations on effective pressures and strongly related to microstructures and fluid inclusions. With the extensive publications, the elastic nonlinearity of rocks due to the presence of compliant mechanical defects (cracks, microfractures, grain joints) has been well established by experimental measurements (e.g., Zimmerman et al., 1986; Johnson and McCall, 1994; David and Zimmerman, 2012). It is also associated with the rock dilatancy due to fluid deformation (Winkler and McGowan, 2004) and the static deformation of oriented microcracks (Sayers and Ebrom, 1997) as the confining pressure increases. Conventional poro-acoustoelastic theory is based on the Taylor expansion of strain energy functions, assuming homogeneous rocks and neglecting the change of microstructures. The theory has been experimentally confirmed for low-porosity rocks and moderate loading stresses, but fails to describe the nonlinear elastic deformation around compliant pores subject to high loading stresses. The acoustoelastic deformation of porous rocks consists of two different types of energy transformations that are related to grains/stiff pores and compliant pores, respectively, with the latter inducing microstructural changes under high-loading stresses (Berryman and Pride, 1998; Ba et al., 2013).

There have been several prediction models available to describe the elastic nonlinearity. The dual-porosity model (Shapiro, 2003; David and Zimmerman, 2012) is proposed from a well-known three-term conceptual model (Cheng and Toksöz, 1979; Zimmerman et al., 1986; Carcione and Cavallini, 2002; Gei and Carcione, 2003). The model uses a semi-empirical equation to formulate the influence of non-

linear elastic deformations in compliant pores on velocity variations. Under several natural assumptions, it clarifies the physics of several quantities that are attached to the three-term conceptual model. The resultant microstructural-deformation coefficients, however, seem difficult to estimate because of their significant dependence on the stress-induced microstructural change. The dual-porosity model, although simple enough, is a semi-empirical model based on the Taylor expansion, and more importantly, takes no account of the energy transformation of compliant-pore strains. Replacing the Taylor expansion used in the conventional poro-acoustoelastic theory, Fu and Fu (2017) use the Padé expansion to approximate the strain energy function for large-amplitude strains. The resultant Padé poro-acoustoelastic theory can predict the elastic nonlinearity well. However, the Padé coefficients a and b, characterizing the microstructural dependence of elastic constants, may be controversial and need more justification from numerous experimental measurements. An ideal prediction model should not only be able to express the elastic nonlinearity with physically meaningful coefficients, but also explain the energy transformation of compliant-pore strains. The poro-acoustoelastic theory with compliant pores (Fu and Fu, 2018) could be by now the best choice for this purpose. It is formulated by incorporating the dual-porosity model of second-order elastic constants into the conventional poro-acoustoelastic equations by replacing the stress-invariant terms with stress-dependent terms. Considering the strong sensitivity of microcracks to effective stresses, the current study will focus on the dual-porosity third-order elastic constants to describe the elastic nonlinearity with a higher accuracy. The resulting poro-acoustoelastic equations with compliant pores support numerical simulations with high fidelity for ultrasonic wave propagation in prestressed fluid-saturated rocks.

Numerical simulations with digital rocks, bridging the gap between experimental measurements and theoretical predictions, have been confirmed for general applicability to complex rocks. It enables the investigation for the dependence of velocity/attenuation variations on mineral compositions and microstructures. Targeted at numerical wave propagation in poroelastic media, various finite-difference (FD) numerical methods have been extensively studied with poroelastic wave equations (Zhu and McMechan, 1991; Dai et al., 1995; Carcione and Quiroga-Goode, 1995; Carcione and Helle, 1999; Saenger and Shapiro, 2002; Wang et al., 2003; Mason et al., 2006; Wenzlau and Müller, 2009). Hu et al. (2009) present a boundary-element modeling of Biot's poroelastic integral equations at seismic frequencies for fluid saturated porous media. Most of these studies focus on the accuracy and applicability of poroelastic numerical schemes. It is worth mentioning that poroelastic numerical modeling has been used to investigate the effect of partial saturations (Pham et al., 2002; Carcione et al., 2003a; Helle et al., 2003; Picotti et al., 2007) and rock heterogeneities (Carcione and Picotti, 2006). A comprehensive review of poroelastic numerical modeling with mathematical details can be referred to Carcione (2007). However, most of the poroelastic numerical studies are based on conceptual rheological models, disenabling a comparison with experimental measurements of real cores. Gurevich (1996) suggest that all numerical simulations based on the complex rheological models should be compared to an equivalent elastic model. This invokes the comparison of poroelastic effects between experimental and numerical data. Gurevich et al. (1999) compare experiments on a sample made of sintered glass beads to synthetic seismograms by a global matrix approach. Arntsen and Carcione (2001) simulate the Biot slow wave based on the experimental data (Kelder and Smeulders, 1997) in water-saturated Nivelsteiner Sandstone. Currently, digital core technologies based on X-ray tomography can capture the mineral components and microstructures of a sample at micrometer resolution, making it possible to simulate poroelastic wave propagation in authentic heterogeneous rocks for the comparison with experimental measurements (Fu et al., 2014; Zhang et al., 2014).

In the current study, we present a poro-acoustoelastic numerical modeling of ultrasonic waves in prestressed, digital, and heterogeneous fluid-saturated rocks. The poro-acoustoelastic numerical simulation is more natural than conventional poroelastic numerical simulations for ultrasonic wave propagation in prestressed porous rocks. Although micro-tomographic images can map rock properties in detail, including both pore and grain structures, several key issues really challenge the comparison of numerical simulations with experimental measurements: (1) the digital model of poroelastic properties that characterizes true rocks in both mineral compositions and microstructures, (2) the estimation of poro-acoustoelastic constants that accounts for the elastic nonlinearity of rocks due to compliant pores under large-magnitude stresses, (3) the high accuracy to model subtle transmission/scattering effects across pores and grains with minimal numerical dispersions at high frequencies and strong heterogeneities, and (4) the special requirement for a controllable and accurate absorbing boundary to estimate the amount of boundary reflections from the side ends of a sample in the experimental environment.

Poroelastic numerical modeling has been widely used for digital cores (Garboczi and Day, 1995; Roberts and Garboczi, 2000; Arns et al., 2002; Dvorkin et al., 2011, 2012; Zhang et al., 2016). For general applicability to complex rocks, we use a finite-element (FE) method to estimate the poroelastic properties from a heterogeneous digital core. The resulting poroelastic model allows its physical properties to vary laterally and vertically, mapping heterogeneous rock

properties in detail. For ultrasonic wave propagation, a modified FE method (Meng and Fu, 2017) is employed to discretize the poro-acoustoelastic equations with compliant pores. We use triangular elements to mesh the digital poroelastic model, with its accuracy controllable to simulate the subtle effect of microstructures on ultrasonic wave propagation in prestressed fluid-saturated rocks. The nonlinear poro-acoustoelastic constants are estimated by the prediction model (Fu and Fu, 2018) through experimental measurements, accounting for the elastic nonlinearity of rocks due to compliant pores under large-magnitude stresses. The perfectly matched layer (PML) absorbing boundary is employed in the simulation to investigate the influence of boundary reflections on ultrasonic coda waves.

In this paper, we outline a general procedure for the poro-acoustoelastic FE modeling with compliant pores for ultrasonic wave propagation. In the second section, we incorporate the dual-porosity model into conventional poro-acoustoelasticity theory to account for nonlinear deformations in compliant pores under large-magnitude stresses. Section 3 introduces laboratory ultrasonic measurements for a fluid-saturated sandstone core along the stress path under a constant confining pressure of 65 MPa with pore pressure increasing from 5 to 60 MPa at an increment of 5 MPa. Based on the experimental ultrasonic data, we demonstrate how to estimate the nonlinear poro-acoustoelastic constants. Section 4 deals with poroelastic FE numerical modeling of elastic properties from digital rock images. The sandstone used for experimental measurements in Section 3 is scanned by X-ray CT to obtain digital images. Based on the scale of pores and grains, we assess the heterogeneity of the digital poroelastic model by calculating its scattering intensity using some random medium methods. These stochastic characteristics are useful for the interpretation of scattering attenuation in simulated ultrasonic waves. The final section presents poro-acoustoelastic FE modeling of ultrasonic waves based on the digital poroelastic model, followed by the comparison with experimental measurements in both waveform and coda attenuation.

2. Poro-acoustoelasticity with compliant pores

Experimental measurements have been demonstrated that the work of loading stress is transformed to strain energy by two parts: one for grains and stiff pores with the linear variation of elastic moduli and the other for compliant pores with the nonlinear variation of elastic moduli (e.g., Cheng and Toksöz, 1979; Shapiro, 2003; Fu and Fu, 2018). Conventional poro-acoustoelasticity is based on the third-order elastic constants and generally valid for the former by neglecting the effect of nonlinear deformations with compliant pores. The elastic nonlinearity occurring at larger loading stresses leads to exponential changes in experimental elastic wave velocities (Winkler and Liu, 1996; Gurevich et al., 2010; Pervukhina et al., 2010). Fu and Fu (2018) incorporate the dual-porosity model into the second-order elastic constants to account for the elastic nonlinearity of compliant pores. For more accurate poro-acoustoelastic prediction, we incorporate the dual-porosity model into the third-order elastic constants. The modified poro-acoustoelasticity becomes more accurate to express the nonlinear elastic deformation in compliant pores subject to high loading stresses.

2.1 The dual-porosity third-order elastic constants

Shapiro (2003) explains the stress-dependent elastic properties of porous rocks in terms of a dual distribution of porosity, where the total porosity (ϕ) of an isotropic rock can be divided into two parts: stiff porosity (ϕ_s) and compliant porosity (ϕ_c). With the extensive publications, the definition of stiff and compliant pores has been well established (Cheng and Toksöz, 1979; Thomsen, 1995; Hudson et al., 2001; Gurevich et al., 2010; David and Zimmerman, 2012; Guéguen and Sarout, 2011). The stiff porosity is supported by more or less isometric pores (i.e., equidimensional or equant pores) with the aspect ratios (γ) typically larger than 0.01, whereas the compliant porosity is supported by thin cracks and grain contact vicinities with the aspect ratios less than 0.01. That is, the porosity can be written as

$$\phi = \phi_s + \phi_c. \tag{1}$$

Variations in ϕ_s and ϕ_c with the effective pressure P can be expressed as

$$\begin{cases} \phi_s = \phi_{s0} + P\left(C_{gr} - C_{drs}\right), \\ \phi_c = \phi_{c0}\exp(-\theta_c P C_{drs}), \end{cases} \tag{2}$$

where ϕ_{s0} and ϕ_{c0} are the initial stiff and compliant porosities at $P = 0$, respectively, and the compliant-pore bulk strain θ_c is defined by

$$\theta_c = \frac{1}{C_{drs}}\frac{\partial C_{dr}}{\partial \phi_c}. \tag{3}$$

C_{dr}, C_{gr}, and C_{drs} are the bulk compressibilities of dry rock skeleton, rock matrix, and dry rock skeleton when $\phi_c \to 0$, respectively, given by

$$\begin{cases} C_{dr} = \dfrac{1}{K_{dr}}, \\ C_{gr} = \dfrac{1}{K_{gr}}, \\ C_{drs} = \dfrac{1}{K_{drs}}, \end{cases} \tag{4}$$

where K_{dr} and K_{gr} are the bulk moduli of dry rock skeleton and rock matrix, respectively, and K_{drs} is the drained bulk modulus of a rock with closed compliant pores.

Variations in the elastic parameter Λ (e.g., seismic velocity, stiffness, or compliance) with stiff and compliant porosities are generally given by (Shapiro, 2003; Shapiro and Kaselow, 2005),

$$\Lambda(\phi_s, \phi_c) = \Lambda_{drs} + \theta_{s\Lambda}\Delta\phi_s + \theta_{c\Lambda}\phi_c, \tag{5}$$

where Λ_{drs} is the stiff limit elastic parameter of dry rock skeleton when $\phi_c \to 0$. $\Delta\phi_s = \phi_s - \phi_{s0}$ is the deviation of stiff porosity. $\theta_{s\Lambda}$ and $\theta_{c\Lambda}$ are the pressure-sensitivity coefficients for stiff and compliant pores, respectively, defined by

$$\begin{cases} \theta_{s\Lambda} = \dfrac{\partial\Lambda}{\partial\phi_s}, \\ \theta_{c\Lambda} = \dfrac{\partial\Lambda}{\partial\phi_c}. \end{cases} \tag{6}$$

In general, the influence of stiff pores is associated with linear elastic deformations, whereas the contribution of compliant pores mainly involves nonlinear strains (Shapiro and Kaselow, 2005). The elastic parameter of rocks due to compliant pores for small variations in ϕ_c can be approximated as

$$\Lambda(\phi_c) = \Lambda_{drs} + \theta_{c\Lambda}\phi_c. \tag{7}$$

Substituting eq. (2) into eq. (7) yields

$$\Lambda(\phi_c) = \Lambda_{drs} + \theta_{c\Lambda}\phi_{c0}\exp(-\theta_c PC_{drs}). \tag{8}$$

We consider the second- and third-order elastic constants in the initial state. Thus, with the influence of prestressed compliant pores, both the elastic constants of rocks become

$$\begin{cases} c_{IJKL}(\phi_c) = c_{IJKL}^{drs} + \theta_{cc_{IJKL}}\phi_{c0}\exp\left(-\theta_c PC_{drs}\right), \\ c_{IJKLMN}(\phi_c) = c_{IJKLMN}^{drs} + \theta_{cc_{IJKLMN}}\phi_{c0}\exp\left(-\theta_c PC_{drs}\right), \end{cases} \tag{9}$$

with

$$\begin{cases} \theta_{cc_{IJKL}} = \dfrac{\partial c_{IJKL}}{\partial\phi_c}, \\ \theta_{cc_{IJKLMN}} = \dfrac{\partial c_{IJKLMN}}{\partial\phi_c}, \end{cases} \tag{10}$$

where c_{IJKL}^{drs} and c_{IJKLMN}^{drs} are the second- and third-elastic constants of dry rock skeleton when $\phi_c \to 0$, respectively. We define θcc_{IJKL} and θcc_{IJKLMN} as the pressure-sensitivity coefficients for the second- and third-order elastic constants of compliant pores, respectively. The order of magnitudes of θc and θcc_{IJKL} can be obtained by various effective medium theories of elastic moduli for the rock with penny-shaped cracks (Mavko et al., 2009), with all coinciding in the case of $\phi_c \to \infty$ by the method of Shapiro (2003). That is, θcc_{IJKL} and θcc_{IJKLMN} are usually on the magnitude order of $1/\gamma$. Thus, we have

$$\begin{cases} \theta_c \propto \left|\dfrac{K_{drs}}{\gamma}\right|, \\ \theta_{cc_{IJKL}} \propto \left|\dfrac{c_{IJKL}^{dry}}{\gamma}\right|, \\ \theta_{cc_{IJKLMN}} \propto \left|\dfrac{c_{IJKLMN}^{dry}}{\gamma}\right|. \end{cases} \tag{11}$$

Based on the studies of David and Zimmerman (2012) and Deng et al. (2015), the minimum initial compliant-pore aspect ratio versus differential pressures can be expressed as

$$\gamma^i = \frac{4\left(1-\nu_{drs}^2\right)}{\pi E_{drs}}P, \tag{12}$$

where E_{drs} and ν_{drs} are the static Young's modulus and Poisson's ratio of dry rocks when $\phi_c \to 0$, respectively. In general, the order of magnitude of γ^i is the same as that of γ (David and Zimmerman, 2012; Deng et al., 2015). Their discrepancy could be small enough to be neglected with the same effective medium model under the same order of magnitude of compliant-pore aspect ratios. Therefore, we assume

$$\gamma \approx \gamma^i = \frac{4\left(1-\nu_{drs}^2\right)}{\pi E_{drs}}P. \tag{13}$$

Equation (13) indicates the correlation of variations in the aspect ratios of compliant pores with effective pressures. In general, the extension deformation of compliant pores with increasing effective stresses reduces aspect ratios (David and Zimmerman, 2012), leading to the closure of compliant pores.

Based on the compliant-pore influence on elastic constants as shown in eq. (8), we can formulate the stress-induced elastic constants (L, μ, K, M_5, M_6), expressed as

$$\begin{cases} L = L_{drs} + \theta_{cL}\phi_{c0}\exp(-\theta_c PC_{drs}), \\ \mu = \mu_{drs} + \theta_{c\mu}\phi_{c0}\exp\left(-\theta_c PC_{drs}\right), \\ K = K_{drs} + \theta_{cK}\phi_{c0}\exp(-\theta_c PC_{drs}), \\ M_5 = M_5^{drs} + \theta_{cM_5}\phi_{c0}\exp\left(-\theta_c PC_{drs}\right), \\ M_6 = M_6^{drs} + \theta_{cM_6}\phi_{c0}\exp\left(-\theta_c PC_{drs}\right), \end{cases} \tag{14}$$

with

$$\begin{cases} \theta_{cL} = \dfrac{\partial L}{\partial\phi_c}, \\ \theta_{c\mu} = \dfrac{\partial\mu}{\partial\phi_c}, \\ \theta_{cK} = \dfrac{\partial K}{\partial\phi_c}, \\ \theta_{cM_5} = \dfrac{\partial M_5}{\partial\phi_c}, \\ \theta_{M_6 c} = \dfrac{\partial M_6}{\partial\phi_c}. \end{cases} \tag{15}$$

These microstructural-deformation coefficients characterize the third-order elastic constants and are sensitivity to compliant porosity changes. Like the second-order elastic constants of Shapiro (2003), these parameters are relevant to the geometry and composition of microstructures. However similar to the dual-porosity model of Shapiro (2003) and David and Zimmerman (2012), these parameters seem difficult to estimate because of their significant dependence on the stress-induced change of microstructures. More accurate estimation could be obtained first by X-ray CT scanning the prestressed rock sample to capture the stress-induced change of compliant pores in detail, then by applying some effective-medium approximations to the resulting digital core. However, for current study, we focus on poro-acoustoelastic FE modeling, with the microstructural-deformation coefficients known in advance. For an accurate estimation of these coefficients to assure the comparison of numerical simulations and experimental measurements, the best fitting is adopted to experimental measurements, addressed in the next section.

As for the effect of nonlinear deformations on the elastic moduli, as demonstrated in eq. (14), we rewrite the strain of rocks in the form

$$e_0^i = -\frac{P}{3[K_{drs}+\theta_{Kc}\phi_{c0}\exp(-\theta_c PC_{drs})]}. \tag{16}$$

With $P\to\infty$, we have

$$\begin{cases} L \to L_{drs}, \\ \mu \to \mu_{drs}, \\ K \to K_{drs}, \\ M_5 \to M_5^{drs}, \\ M_6 \to M_6^{drs}, \\ \phi_c \to 0. \end{cases} \tag{17}$$

Equation (17) indicates that the second- and third-order elastic constants tend to be constants against effective pressure since the compliant porosity decreases to zero. Therefore, the influence of compliant pores can be neglected at the limit of high effective pressures (i.e., with low pore pressures).

2.2 Poro-acoustoelasticity for the elastic nonlinearity of compliant pores

From Appendix A (https://link.springer.com), we see that conventional poro-acoustoelasticity assumes the parameters, such as elastic constants, porosities, densities and so on, to be constants during the loading. That is, rock microstructures remain unchanged. This assumption is valid for a small-magnitude loading. As indicated by eq. (A-10) in Appendix A, the conventional poro-acoustoelasticity provides an analytical expression for the effective elastic moduli of rocks, as functions of elastic strains for small changes in stress. In general, the second- and third-order elastic constants (L, μ, K, M_5, and M_6) are dependent on microstructures (Berryman and Pride, 1998), and therefore experience nonlinear deformations induced by high loading stresses. Based on the dual-porosity model with the third-order elastic constants, described previously for nonlinear elastic deformations, we modify the classical poro-acoustoelasticity by representing the elastic constants as functions of stress to build an analytical expression of effective elastic moduli for large-magnitude changes in stress.

According to the dual-porosity model, both the linear and nonlinear elastic influences on rocks can be linearly superposed for small compliant porosities. The stress-induced variations in the effective elastic modulus consist of linear and nonlinear components, with the former calculated by the conventional acoustoelasticity and the latter handled by the dual-porosity third-order elastic constants, as expressed by eq. (14). Substituting eqs. (14) and (16) into eq. (A-10), the modified acoustoelasticity with compliant pores can be formulated as,

$$\begin{cases} D_{11}(P) = \rho V_P^2 = L_{drs} + \theta_{cL}\phi_{c0}\exp(-\theta_c PC_{drs}) + \left[M_5^{drs} + \theta_{cM_5}\phi_{c0}\exp\left(-\theta_c PC_{drs}\right)\right]\dfrac{P}{3[K_{drs}+\theta_{cK}\phi_{c0}\exp(-\theta_c PC_{drs})]}, \\ D_{33}(P) = \rho V_P^2 = L_{drs} + \theta_{cL}\phi_{c0}\exp(-\theta_c PC_{drs}) + \left[M_5^{drs} + \theta_{cM_5}\phi_{c0}\exp\left(-\theta_c PC_{drs}\right)\right]\dfrac{P}{3[K_{drs}+\theta_{cK}\phi_{c0}\exp(-\theta_c PC_{drs})]}, \\ D_{55}(P) = \rho V_S^2 = \mu_{drs} + \theta_{c\mu}\phi_{c0}\exp(-\theta_c PC_{drs}) + \left[M_6^{drs} + \theta_{cM_6}\phi_{c0}\exp\left(-\theta_c PC_{drs}\right)\right]\dfrac{P}{3[K_{drs}+\theta_{cK}\phi_{c0}\exp(-\theta_c PC_{drs})]}, \\ D_{13} = D_{11} - 2D_{55}, \\ D_{51} = 0, \\ D_{53} = 0. \end{cases} \tag{18}$$

According to eqs. (11) and (15), we assume

$$\begin{cases}\theta_{cL}=\dfrac{\partial L}{\partial\phi_c}=\dfrac{a}{\gamma},\\ \theta_{c\mu}=\dfrac{\partial \mu}{\partial\phi_c}=\dfrac{b}{\gamma},\\ \theta_{cK}=\dfrac{\partial K}{\partial\phi_c}=\dfrac{c}{\gamma},\\ \theta_{c}=\dfrac{1}{C_{drs}}\dfrac{\partial C_{dr}}{\partial\phi_c}=\dfrac{d}{\gamma},\\ \theta_{cM_5}=\dfrac{\partial M_5}{\partial\phi_c}=\dfrac{e}{\gamma},\\ \theta_{cM_6}=\dfrac{\partial M_6}{\partial\phi_c}=\dfrac{f}{\gamma},\end{cases}\tag{19}$$

with

$$\begin{cases}|a|\propto|b|\propto|c|\propto c_{IJKL}^{drs},\\ |d|\propto K_{drs},\\ |e|\propto|f|\propto c_{IJKLMN}^{drs},\end{cases}\tag{20}$$

where the microstructural-deformation coefficients a, b, c, d, e, and f have the same physical meaning as their counterparts, but become more sensitive to stress-induced microstructural changes and therefore, easy to estimate by best fitting to ultrasonic measurements.

Equations (18) to (20) represent the poro-acoustoelasticity with compliant pores, where the exponential dependence of the third-order elastic constants on effective pressures is characteristic of the nonlinear influence of compliant pores. When the effective pressure P tends to infinity, eq. (18) reduces to

$$\begin{cases}D_{11}(\infty)=L_{drs}+M_5^{drs}\dfrac{P}{3K_{drs}},\\ D_{33}(\infty)=L_{drs}+M_5^{drs}\dfrac{P}{3K_{drs}},\\ D_{55}(\infty)=\mu_{drs}+M_6^{drs}\dfrac{P}{3K_{drs}},\\ D_{13}(\infty)=D_{11}(\infty)-2D_{55}(\infty),\\ D_{51}(\infty)=0,\\ D_{53}(\infty)=0.\end{cases}\tag{21}$$

Equation (21) denotes the upper limit of the poro-acoustoelasticity with compliant pores under higher effective pressures. In the case of the maximum effective pressure, all compliant pores tend to be closed, increasing the stiffness of rocks and decreasing the permeability (Schoenberg, 2002). With decreasing nonlinear deformations, the poro-acoustoelasticity with compliant pores reduces to conventional poro-acoustoelasticity.

3. Laboratory ultrasonic measurements for the estimation of nonlinear poro-acoustoelastic constants

Laboratory ultrasonic measurements for a cylindrical fluid-saturated sandstone sample under different effective pressures are employed to illustrate the applicability of poro-acoustoelastic modeling with compliant pores. Compared to the dual-porosity second-order elastic constants (Fu and Fu, 2018), the dual-porosity third-order elastic constants are demonstrated to be more precise for the prediction of elastic nonlinearity due to compliant pores.

3.1 Experimental setup and rock properties

A schematic diagram of the ultrasonic measurement system is shown in Figure 1. The experimental setup consists of a pulse generator (Panametrics 5077PR) and a digital oscilloscope (Tektronix TDS 420 A). Ultrasonic compressional and shear waves with a characteristic frequency of 1 MHz are emitted from the pulse generator in a PZT-crystal mounted on the steel endplate. The receiving transducer is connected to the digitizing board in a PC through a signal amplifier. The characteristic frequencies of received compressional and shear waves are approximately 600 and 300 kHz, respectively, because of the attenuation within the sample. The amplitudes of transmitted elastic waves are monitored by the digital oscilloscope at the opposite side of the sample. Referring to ASTM standard (American Society for the Testing of Materials, 2002), the length-to-diameter ratio of a rock specimen is recommended between 2 and 2.5 to avoid end constraint effects (Franklin and Dusseault, 1989). Therefore, the rock sample is cut to a cylinder with 40 mm in diameter and 80 mm in length. The resulting specimen is jacketed with rubber tubing to isolate it from the oil which provides confining pressure. A pore fluid inlet presents in each endplate to allow the passage of pore fluids through the sample. The experiment is performed under ambient pressure conditions along the stress path with a constant confining pressure of 65 MPa and increasing pore pressures from 5 to 60 MPa (using water as the pore fluid) at an increment of 5 MPa. Waveforms are recorded after pore-pressure equilibration at each effective stress increment.

The sample used is a medium-porosity (19%), moderate-permeability (41 mD) quartz sandstone with the static bulk modulus K = 13.20 GPa, the static Young's modulus E = 14.26 GPa, ν = 0.32, and ρ = 2.27 g cm^{-3}, all measured at P = 60 MPa. Figure 2 gives a close up of the center of the sandstone sample, showing microstructures with various sizes of quartz grains and pores. It consists of moderately sorted, subangular to subrounded quartz grains (0.1–0.3 mm in diameter) with point contacts one another. Pore size varies from about 0.1 mm to about 0.4 mm. Most grains and pores are around 0.2 mm in size. Minor clays and glauconites that are present generally reside in pores. Most grain boundaries are direct contacts between rigid framework grains. Intragrain fractures are rare, but grain boundaries and cracks are ubiquitous. These fracture surfaces, grain boundaries,

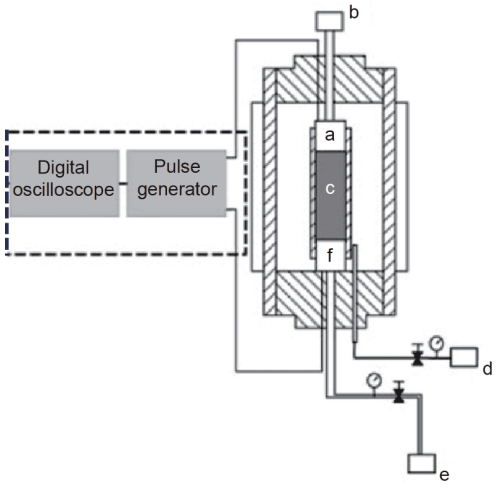

Figure 1 Schematic of the experimental apparatus. a, Transmitting piezoelectric transducer; b, pore fluid inlet; c, jacketed rock sample; d, confining pressure control; e, downstream pore fluid outlet; f, receiving piezoelectric transducer.

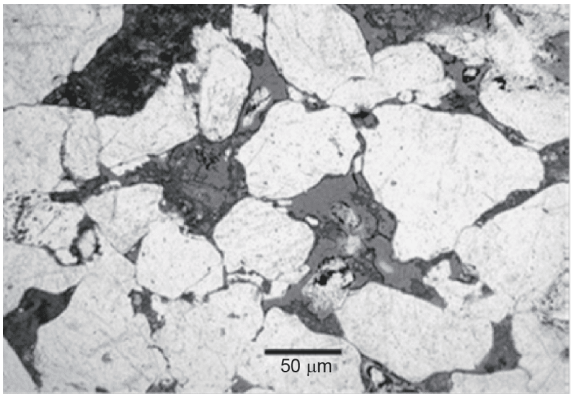

Figure 2 Close up of the center of the sandstone sample under study, showing microstructures with various sizes of quartz grains and pores.

microcracks, and contact faces between grains are all sensitive to stress and generally constitute the compliant microstructure. The observed *P*- and *S*-wave velocities are plotted against effective stress in Figure 3. The arrival-time pick is based on the first break estimated from approximately 1% of the first peak amplitude.

3.2 Estimation of poro-acoustoelastic constants

Equation (18) will be used for poro-acoustoelastic FE modeling for ultrasonic wave propagation. We first estimate the parameters (L_{drs}, μ_{drs}, M_5^{drs}, M_6^{drs}) in eq. (18) through experimental measurements. We investigate the stress dependency of these parameters.

As shown in Figure 4, the observed ultrasonic data from experimental measurements addressed in Section 3.1 demonstrate a distinct behavior of elastic moduli in the low and high regimes of effective pressures. The variation of elastic moduli versus effective pressure shows a linear/nonlinear trend for the effective pressures greater/less than 30 MPa, as marked by a line in the figure. The linear portion conforms to the prediction of effective elastic moduli by conventional poro-acoustoelasticity, assuming that the microstructures in rocks tend to be stable with almost unchanged heterogeneities under loading with the effective-pressure points greater than 30 MPa. Under such circumstances, compliant pores tend to be closed with the nonlinear effect could be neglected. We can use these measurements at the high effective-pressure points to calculate the elastic constants (L_{drs}, μ_{drs}, M_5^{drs}, M_6^{drs}).

Based on eq. (21) for the upper limit of acoustoelasticity with compliant pores under high effective pressures, we could use the measurements at the two largest effective-pressure points of $P = 50$ and 60 MPa to solve out four elastic constants (L_{drs}, μ_{drs}, M_5^{drs}, M_6^{drs}). First, we assume that the quartz sandstone at $P = 60$ MPa contains only stiff pores with closed compliant pores. Based on the static parameters of $K = 13.20$ GPa, $E = 14.26$ GPa, $\nu = 0.32$, and $\rho = 2.27$ g cm^{-3}, all measured at $P = 60$ MPa, we have

$$\begin{cases} K_{drs} \approx K|_{P=60\ \mathrm{MPa}} = 13.20\ \mathrm{GPa}, \\ E_{drs} \approx E|_{P=60\ \mathrm{MPa}} = 14.26\ \mathrm{GPa}, \\ \nu_{drs} \approx \nu|_{P=60\ \mathrm{MPa}} = 0.32. \end{cases} \tag{22}$$

Secondly, substituting the measured velocities at $P = 50$

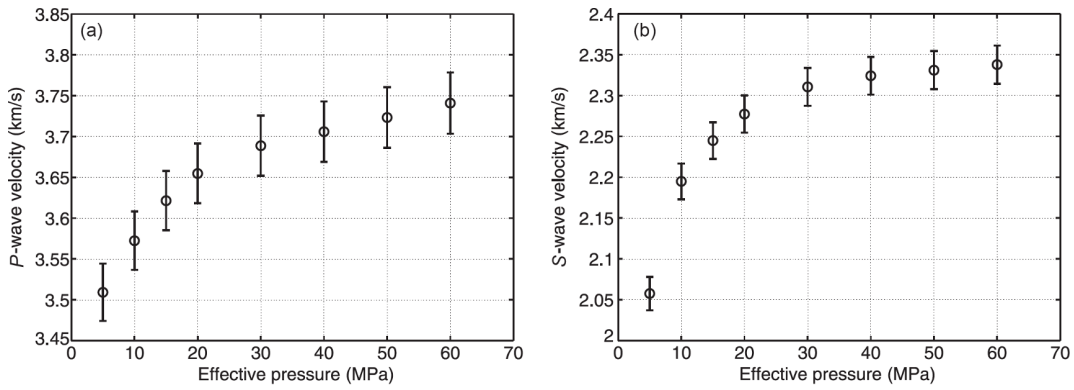

Figure 3 The observed *P*- and *S*-wave velocities against effective stress for the sandstone core.

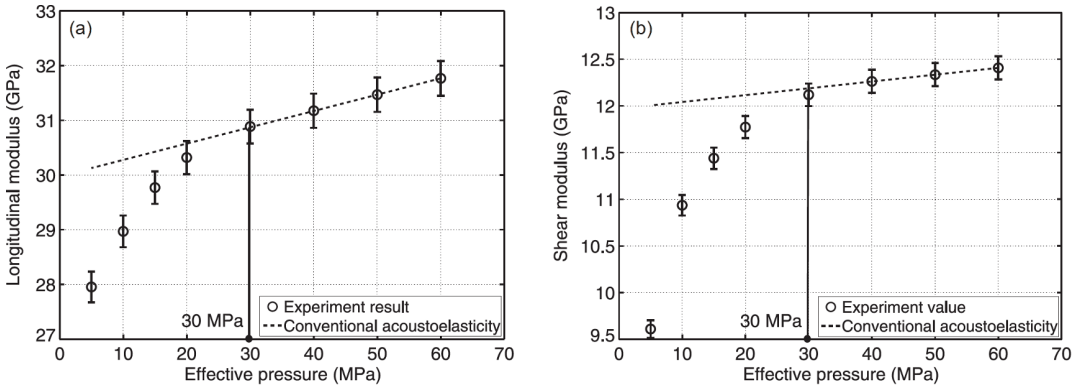

Figure 4 Variations of longitudinal (a) and shear (b) elastic moduli versus effective pressure, with the conventional poro-acoustoelasticity prediction (dotted lines) for linear elastic deformations.

and 60 MPa into eq. (A-10), we have

$$\begin{cases} D_{11}|_{P=60\,\mathrm{MPa}} = D_{33}|_{P=60\,\mathrm{MPa}} = \rho V_P^2|_{P=60\,\mathrm{MPa}} = 31.77\ \mathrm{GPa}, \\ D_{11}|_{P=50\,\mathrm{MPa}} = D_{33}|_{P=50\,\mathrm{MPa}} = \rho V_P^2|_{P=50\,\mathrm{MPa}} = 31.47\ \mathrm{GPa}, \\ D_{55}|_{P=60\,\mathrm{MPa}} = \rho V_S^2|_{P=60\,\mathrm{MPa}} = 12.41\ \mathrm{GPa}, \\ D_{55}|_{P=50\,\mathrm{MPa}} = \rho V_S^2|_{P=50\,\mathrm{MPa}} = 12.33\ \mathrm{GPa}. \end{cases} \tag{23}$$

Substitution of eq. (23) into eq. (21) gives the following expression for the effective elastic moduli (D_{11}, D_{55}),

$$\begin{cases} D_{11}|_{P=60\,\mathrm{MPa}} = D_{33}|_{P=60\,\mathrm{MPa}} = L_{drs} - M_5^{drs}\dfrac{P|_{P=60\,\mathrm{MPa}}}{3K_{drs}}, \\ D_{11}|_{P=50\,\mathrm{MPa}} = D_{33}|_{P=50\,\mathrm{MPa}} = L_{drs} - M_5^{drs}\dfrac{P|_{P=50\,\mathrm{MPa}}}{3K_{drs}}, \\ D_{55}|_{P=60\,\mathrm{MPa}} = \mu_{drs} - M_6^{drs}\dfrac{P|_{P=60\,\mathrm{MPa}}}{3K_{drs}}, \\ D_{55}|_{P=50\,\mathrm{MPa}} = \mu_{drs} - M_6^{drs}\dfrac{P|_{P=50\,\mathrm{MPa}}}{3K_{drs}}. \end{cases} \tag{24}$$

By substituting eq. (23) into eq. (24), we obtain an equation for the elastic constants (L_{drs}, μ_{drs}, M_5^{drs}, M_6^{drs}),

$$\begin{cases} L_{drs} - 1.52\times10^{-3}M_5^{drs} = 31.77\ \mathrm{GPa}, \\ L_{drs} - 1.26\times10^{-3}M_5^{drs} = 31.47\ \mathrm{GPa}, \\ \mu_{drs} - 1.52\times10^{-3}M_6^{drs} = 12.41\ \mathrm{GPa}, \\ \mu_{drs} - 1.26\times10^{-3}M_6^{drs} = 12.33\ \mathrm{GPa}. \end{cases} \tag{25}$$

By solving eq. (25), we have

$$\begin{cases} L_{drs} = 29.98\ \mathrm{GPa}, \\ \mu_{drs} = 11.97\ \mathrm{GPa}, \\ M_5^{drs} = -1180.91\ \mathrm{GPa}, \\ M_6^{drs} = -289.59\ \mathrm{GPa}. \end{cases} \tag{26}$$

These elastic constants estimated by high effective-pressure measurements can be used in eq. (18) to predict the partial variation of elastic moduli induced by linear elastic deformations in the sample, as shown in Figure 4 marked by the dotted lines. These high effective pressures make acoustoelasticity with compliant pores approach its upper limit, as shown in eq. (21).

3.3 Estimation of microstructural coefficients

To assure the comparison of numerical simulations and experimental measurements, we need an accurate estimation of microstructural coefficients. The best fitting of experimental measurements is performed for the estimation of microstructural-deformation coefficients (a, b, c, d, e, f, and ϕ_{c0}) in eq. (19). The results are listed in Table 1, by which we perform poro-acoustoelastic predictions with/without compliant pores for the effective elastic moduli as functions of effective pressure, as shown in Figure 5.

From the comparison of experimental measurements, conventional poro-acoustoelastic predictions, and poro-acoustoelastic predictions with compliant pores, we see that both the poro-acoustoelastic predictions are nearly the same for the effective pressures higher than 30 MPa, with a prediction error of 1.3%, which characterizes the linear elastic effect of rocks. However, they differ substantially for the effective pressures less than 30 MPa, particularly for shear waves. The poro-acoustoelastic prediction with compliant pores shows a remarkable agreement with experimental measurements, with a 1.8% maximum error at P = 5 MPa, much better than the dual-porosity model with the second-order elastic constants (Fu and Fu, 2018).

These microstructural-deformation coefficients characterize the significant dependence of the third-order elastic constants on stress-induced microstructural changes. In general, fracture surfaces, grain boundaries, microcracks, and joint faces in rocks are all sensitive to stress. Strong hydrostatic stresses tend to compress the pore linings of clays adjacent to framework grain contacts, increasing the stiffness for normal compressions and decreasing the resistance to tangential displacements (Dvorkin et al., 1991). The resultant changes in compliant pores, in turn, affect the second- and

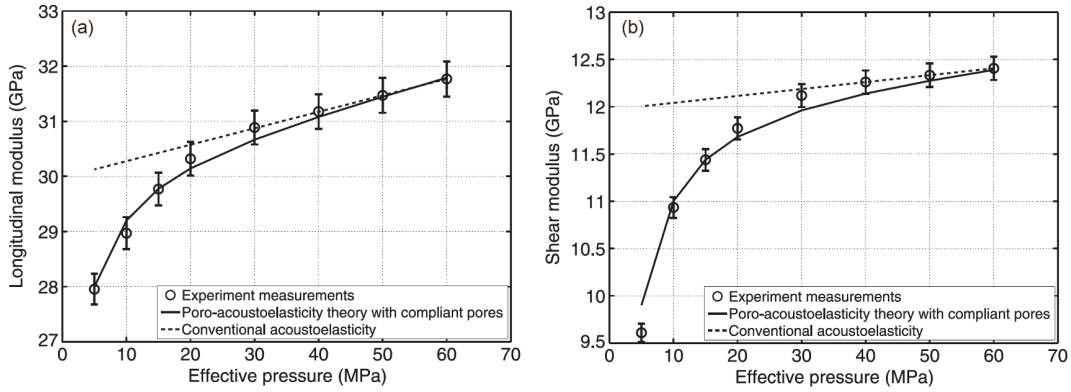

Figure 5 Variations of longitudinal (a) and shear (b) elastic moduli versus effective pressure, with the conventional poro-acoustoelasticity prediction (dotted lines) for linear elastic deformations and the poro-acoustoelasticity prediction (solid lines) with compliant pores for nonlinear elastic deformations.

Table 1 The values of microstructural coefficients for the sandstone core measured

Coefficients	Values
a	–2.50 GPa
b	–2.25 GPa
c	–7.00 GPa
d	0.25 GPa
e	–1700.00 GPa
f	–1300.00 GPa
ϕ_{c0}	0.06%

third-order elastic constants. It is worth mentioning that conventional poroelastic descriptions of the stress dependence of acoustic velocities in rocks are often based on microstructure models. The classical poroelastic theories as a first approximation can handle the stress-induced velocity changes as an anisotropic effect and still obtain a good fit (e.g., Carcione et al., 2003b). A more general solution with model-independent descriptions that ignore microstructures, as indicated by our studies, can be obtained based on the poro-acoustoelastic theory with third-order elastic constants.

4. Numerical experiments for a prestressed, heterogeneous, fluid-saturated, and digital sandstone

As described in Appendix B (https://link.springer.com), we employ a modified FE method (Meng and Fu, 2017) for poro-acoustoelastic modeling with the second-order PML absorbing boundary. The sandstone sample with its observed ultrasonic waveforms described in Section 3 has been extensively studied previously. For example, the stress-associated scattering attenuation is estimated by the single-scattering model based on the weak scattering assumption (Guo and Fu, 2007; Guo et al., 2009). Monte Carlo simulation of stress-associated scattering attenuation (Wei and Fu, 2014) is conducted by minimizing the residual between the observed and synthesized envelopes for all the effective pressures, which indicates that the sandstone sample presents moderate heterogeneities with respect to the used wavelength. Numerical simulation of Biot's poroelastic equations using the digital image of the sample (Fu et al., 2014; Zhang et al., 2014) is approximately implemented to evaluate the effect of boundary reflections from the side ends of a sample core on ultrasonic coda waves in experimental environments. For wave propagation in prestressed porous rocks, it is natural to use poro-acoustoelastic numerical methods. The current study focuses on a general procedure of poro-acoustoelastic FE modeling with compliant pores for prestressed heterogeneous rocks. The observed stress-associated ultrasonic waveforms for this sandstone sample are the best for numerical experiments in this study.

4.1 Setup of digital elastic model

How to create a realistic elastic model as a double-phase medium from digital core images is quite complicated and always controversial because of the correlation of image resolution scales, wavelengths used, and effective medium methods. Improper model settings or errors in numerical elastic properties will destroy the comparison of numerical simulations and experimental measurements. A typical workflow of digital rock physics (DRP) comprises three steps (Saenger et al., 2011): scanning the sample into digital images, separating the pore volume from the matrix phase to obtain segmented images; and predicting volume properties (bulk modulus K, shear modulus μ, as well as density ρ).

The sandstone sample usedis scanned by X-ray CT with a proper resolution, resulting in a huge 3D image data. We select a section along the center line of the cylindrical sample, as shown in Figure 6a with its part magnified into view in Figure 6b. The reconstructed 2D image with a resolution of 0.05 mm is obtained based on the differential absorption to the X-rays, with the grayscale adjusted to show

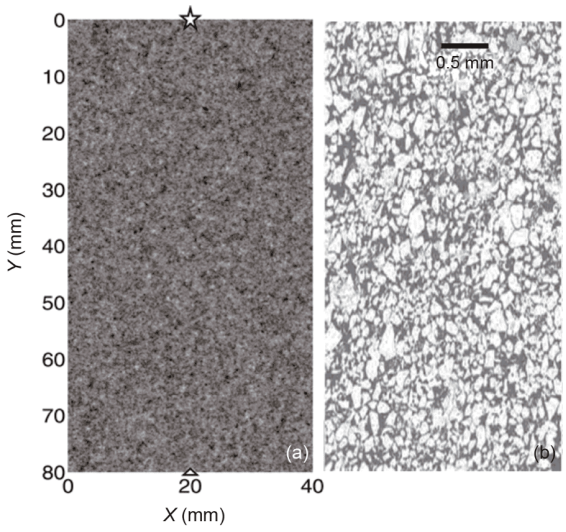

Figure 6 A section of digital cores (a) selected along the center line of the cylindrical sample and its part magnified into view (b), with the white and black colors indicating quartz grains and interstitial clays (pores), respectively. The oil saturated in pores is assumed to fill in the whole background as a double-phase medium. The positions of the source and receiver are indicated by star and triangle, respectively.

different minerals. We see clearly the pore and grain geometries as two major components of the sandstone. It also presents varying amounts of interstitial clays residing in pores. The off-white color indicates quartz grains and the remainder mainly indicates clays residing in pores. For numerical simulations of wave propagation, it seems reasonable to reduce the complex mineral composition into two major components: quartz grains and clays, which basically captures the heterogeneity scale controlled by pore and grain geometries.

We first define proper elastic properties in each pixel point of the model. With such a matrix of digital core images, the volume ratio of two parts, quartz grains and interstitial clays residing in pores, can be easily calculated as 70%:30% averagely. Based on the volume ratio and mineral bulk and shear moduli, we can calculate the equivalent bulk and shear moduli for each pixel by the average modulus estimation (Klimeš, 2002), for more details referred to Zhang et al. (2014).

The key problem is how to convert the digital elastic model into a double-phase medium to make poro-acoustoelastic equations applicable for numerical modeling. Considering that fluids in a real reservoir of oil/gas exist always as a mixture with sands/clays rather than a pure fluid pool. Therefore, water in this study is set to fill in the whole background of the digital core. That is, every point of the model is a mixture of water with either quartz grains or interstitial clays residing in pores, and therefore can be taken as a sort of effective double-phase medium. Such a significant simplification to realistic cores aims to approximate the main characteristics of the true model. Parameters of the digital elastic model are shown in Table 2.

4.2 Heterogeneities of digital elastic model

Digital core with a random distribution of grains and pores is a typical random heterogeneous medium that can be characterized by both direct (e.g., stochastic medium modeling) and indirect (e.g., scaling law of waves) methods. The change of microstructures can be regarded as a kind of small-scale random heterogeneities superposed on the background elastic modulus. In general, the small-scale variations can be estimated by stochastic medium modeling with spatial autocorrelation functions.

For the digital elastic model as shown in Figure 6, the elastic properties can be expressed as

$$\begin{cases} \rho(x,z) = \rho_0\left[1+\varepsilon_\rho(x,z)\right], \ \left\langle \varepsilon_\rho \right\rangle = 0, \\ K(x,z) = K_0[1+\varepsilon_K(x,z)], \ \left\langle \varepsilon_K \right\rangle = 0, \\ \mu(x,z) = \mu_0\left[1+\varepsilon_\mu(x,z)\right], \ \left\langle \varepsilon_\mu \right\rangle = 0, \end{cases} \tag{27}$$

where the spatially mean values (ρ_0, K_0, μ_0) of density, bulk modulus, and shear modulus are superposed by the fluctuations (ε_ρ, ε_K, ε_μ) of elastic properties. As a precondition, the statistical average of the fluctuations ε vanishes. We suppose the spatial random fluctuation $\varepsilon = \varepsilon(x, z)$ is a second-order stationary process with zero mean. Its autocorrelation function can be expressed as functions of variation σ^2 and covariance function $C(x, z)$,

$$\Phi(x,z) = C(x,z)/\sigma^2. \tag{28}$$

Three kinds of autocorrelation functions, Gaussian, exponential, and Von Karman (Klimeš, 2002) have been widely used for stochastic medium models, with each being its own characteristics and suiting for different geological conditions. Based on the shape feature of grains and pores in the digital core shown in Figure 6, we select the following exponential-ellipse autocorrelation function,

Table 2 Physical parameters for the numerical core model

Parameters	K_s (GPa)	K_d (GPa)	μ_s (GPa)	ρ_s (g/cm^3)	ϕ	κ (mD)	v	K_f (GPa)	ρ_f (g/cm^3)	η (Pa S)
Quartz grain	37.00	–	44.00	2.65	–	–	0.08	–	–	–
Clay	25	–	9	2.56	–	–	0.34	–	–	–
Water	–	–	–	–	–	—	–	2.25	1.00	0.001

$$\begin{cases} \Phi(x,z) = \exp\left[-\dfrac{r}{a}\right], \\ r = \sqrt{x^2+z^2}, \end{cases} \tag{29}$$

where the correlation length a depicts the mean scale of heterogeneous abnormalities for an isotopic stochastic medium in the spatial domain. As one of key statistical characteristics, it is strongly related to the sizes of mineral grains and pores in the sample. The correlation length for the sandstone sample under study is estimated through the autocorrelation calculation over all the digital points of Figure 6a. We can identify different minerals in the sample in terms of their X-ray absorptivity. Since the main mineral of sample is quartz, the heterogeneity of sample depends on the size and distribution of quartz grains, i.e., the correlation length. The resulting autocorrelation function is shown in Figure 7 on which we estimate the correlation length as 139.4 μm corresponding to the value of 1/e (e = 2.71828…) in the autocorrelation function Φ.

The mean values of bulk/shear moduli and density at different effective pressures are determined by poro-acoustoelasticity with compliant pores, expressed as

$$\begin{cases} K_0 = D_{11} - \dfrac{4}{3}D_{55}, \\ \mu_0 = D_{55}, \\ \rho_0 = \rho^0, \end{cases} \tag{30}$$

where D_{11} and D_{55} are calculated by eqs. (18) to (20) . Thus, the standard deviation in the random disturbance $\varepsilon = \varepsilon(x, z)$ can be calculated with the normalized disturbance up to σ = 35%. We can reconstruct a digital elastic model based on the mean values (ρ_0, K_0, μ_0), the normalized disturbance σ, and the correlation length a. The model basically reflects the statistical characteristics of its counterpart as shown in Figure 6. The correlation length is the intrinsic property to assess the heterogeneity of digital elastic models. Based on its correlation with wavelengths, which is measured by scaling law, we can examine the scattering intensity for wave propagation in digital elastic models.

Scattering intensity for wave propagation in random heterogeneous media is classified into different regimes, depending upon the parameters ka and kL (Sivaji et al., 2002; Wu and Aki, 1988), where k is the wavenumber and L is the travel distance of waves. Wei and Fu (2014) investigate the scaling law of ultrasonic waves and conduct a rough estimate of a for the same sandstone as used in this study. That is, the correlation length is approximately the averaging size of grains and pores of the sample. The resulting ka-kL distribution diagram indicates that the sample presents moderate heterogeneities with respect to wavelengths used. In this study, we use the exactly estimated correlation length (139.4 μm) to investigate the scattering intensity of the sandstone sample.

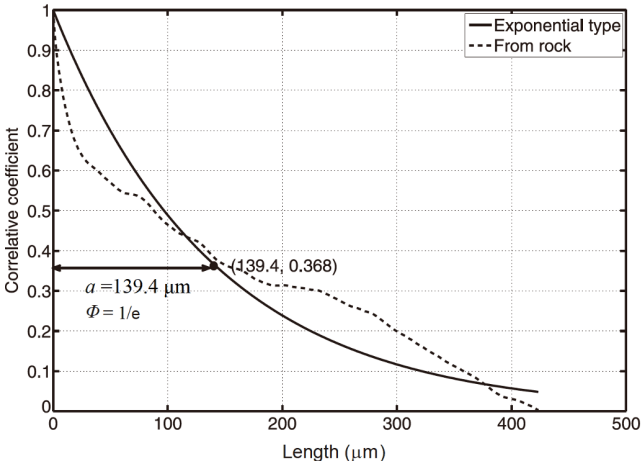

Figure 7 Autocorrelation function of Figure 6a with its correlation length estimated at Φ = 1/e.

For the present experiment, the characteristic frequencies of P- and S-waves are approximately 600 kHz and 300 kHz, respectively, with their velocities of different pore pressures measured by the travel time of direct waves. We choose L = 80 mm (the distance of ultrasonic transmission equaling to the sample length). The calculated ka-kL distribution is shown in Figure 8. We see that the corresponding scale length ka varies from 10^{-2} to 10^{-1} for both P- and S-waves as pore pressure increases from 5 to 60 MPa. Based on the scattering division of the ka-kL distribution (Wu and Aki, 1988), the sample presents moderate to weak scattering strength with respect to wavelengths.

4.3 Numerical experiments with prestressed and fluid-saturated digital elastic model

Comparisons of numerical and experimental ultrasonic waveforms can provide a major impetus to the understanding of detailed characteristics of ultrasonic wave propagation in prestressed heterogeneous rocks. We conduct numerical experiments for the digital elastic model shown in Figure 6, with the source point and receiver located at the positions (20, 80) mm and (20, 0) mm, respectively. The ultrasonic source used for numerical modeling is from the laboratory experiment, as shown in Figure 9, with the center frequencies of 600 kHz and 300 kHz for P- and S-waves, respectively.

Because of the homogenization consideration in the formulation of poro-acoustoelastic equations, the wavelength of numerical experiments must be larger than a typical averaging elementary volume. That is, the wavelength must be at least 10 times larger than the size of grains and pores (Pride et al., 2004; Martin et al., 2008) to avoid some nonphysical behaviors, numerical instabilities, and numerical dispersions appearing in the simulation. Considering the maximum frequency (less than 600 kHz) and the lowest velocity (higher than V_{Smin} = 2000 m s^{-1}) of elastic waves, we compute the

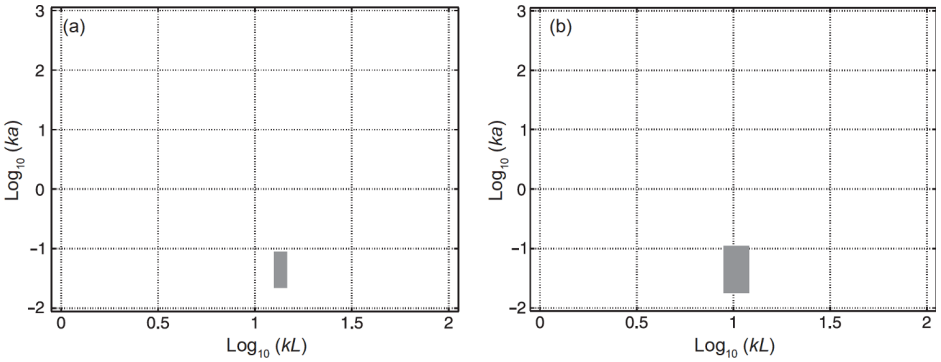

Figure 8 A *ka*-*kL* diagram of scattering intensity with the *P*-wave at *f* =600 kHz (a) and the *S*-wave at *f* = 300 kHz (b) for the sandstone sample under study. The *ka*-*kL* distribution for the present experiment with *a*=139.4 μm, *L* = 80 mm, and the measured velocities, characterizes the heterogeneity scale of the sample with respect to wavelengths, as indicated by a hatched region in the figure.

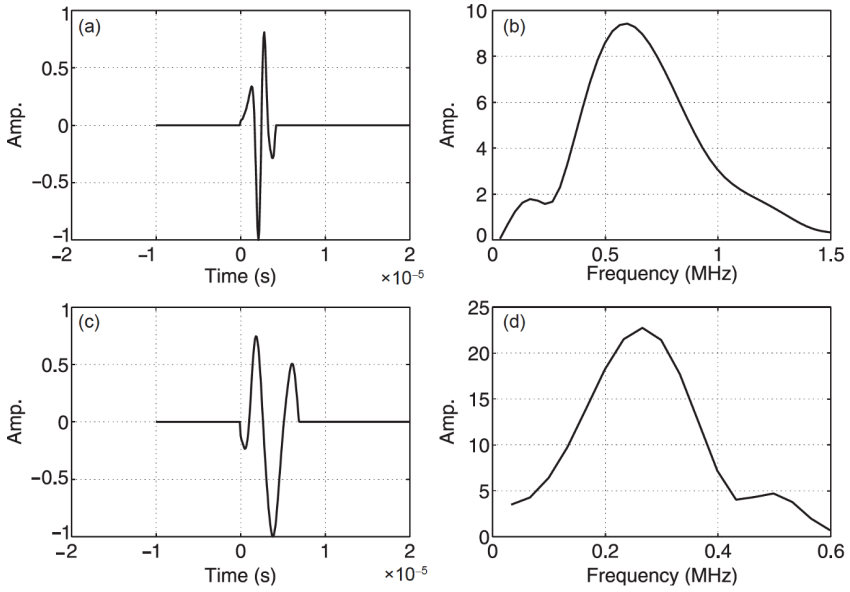

Figure 9 Source wavelets ((a), (c)) with their frequency spectra ((b), (d)) for *P*-waves ((a), (b)) and *S*-waves((c), (d)), respectively.

minimum wavelength as about 2 mm. It is about 40 times the averaging diameter of pores and grains. The minimum edge length h of triangular grid cells is 8×10^{-5} m. From the stability condition (see eq. (B-4) in Appendix B) and the maximum phase velocities ($V_{P\max}$ = 3742.2 m s^{-1} and $V_{S\max}$ = 2336.3 m s^{-1}) of ultrasonic measurements, the time sampling interval of numerical modeling should satisfy $\Delta t \le 8\times10^{-9}$ s. In the current study, we take the time sampling interval Δt = 2×10^{-9} s, in accordance with that of the source. Numerical simulation is performed with 100000 time steps for a total duration of 0.0001 s.

In the simulation, the heterogeneous digital model is surrounded by the PML layer. The radial and vertical components of wavefields are recorded at the receiver. The PML-layer thickness is varied to determine the level of boundary reflections on coda waves by comparing with experimental coda waveforms. Considering the effect of rubber jackets around the sample to weaken boundary reflections to some degree in the laboratory, Fu et al. (2014) compare the numerical and experimental amplitude levels in the ultrasonic coda waveforms, which demonstrates that the boundary reflection from the side ends of a sample core may contribute about one-third of the ultrasonic coda attenuation observed in laboratory experiments. More details for the effect of boundary reflections on coda waves in rock physics experiments can be referred to Fu et al. (2016). The current study focuses on the poro-acoustoelastic FE modeling with compliant pores to assure the agreement between numerical simulations and experimental measurements. For this purpose, we change the PML-layer thickness from 10 to 60 mm in the simulation, and conclude that the 40 mm-thick PML layer is the optimal to assure a consistent amplitude level of ultrasonic coda waves between the numerical and experimental results.

Figure 10 compares the numerical and experimental waveforms for ultrasonic *P*- and *S*-waves at different effective

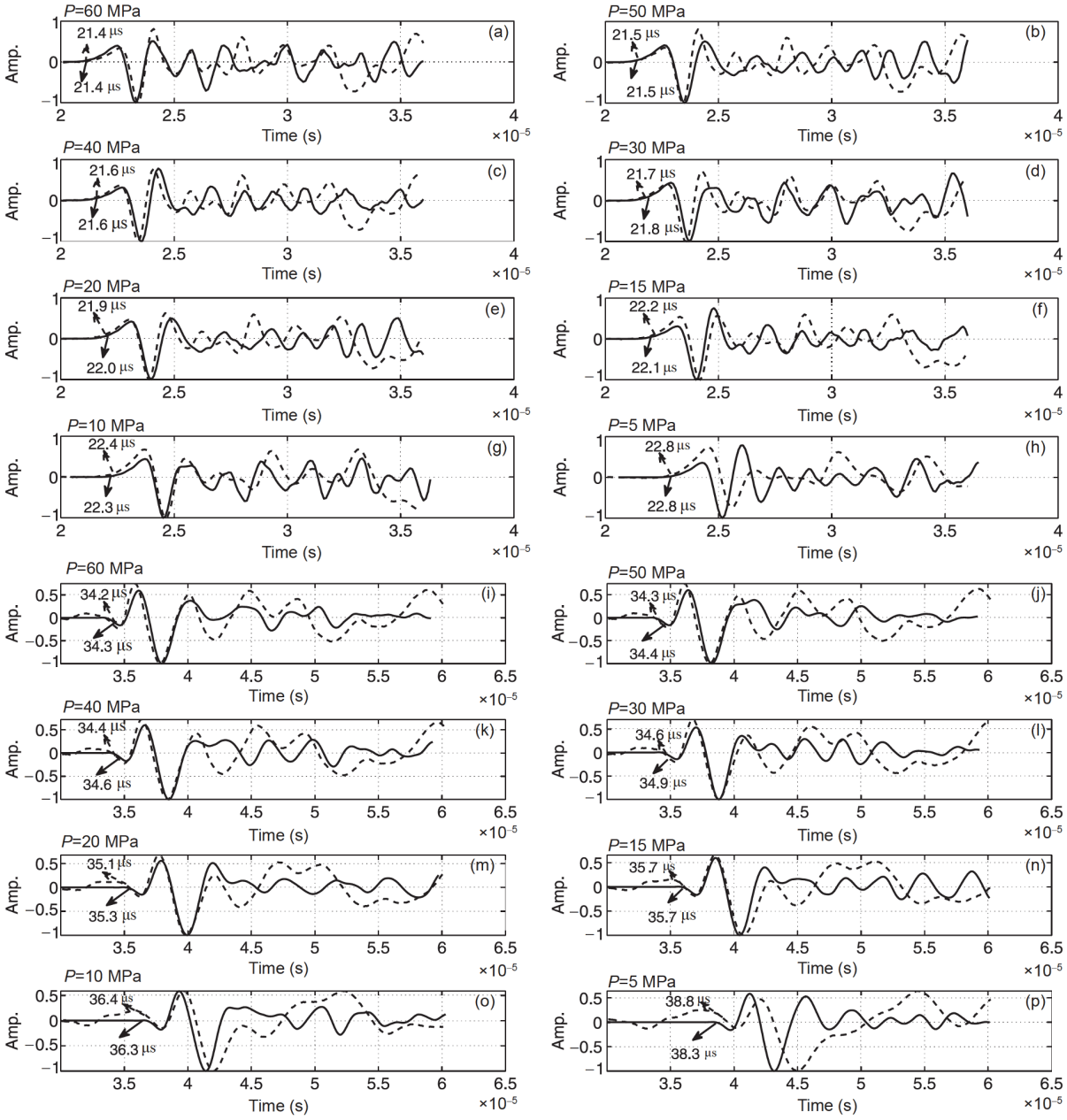

Figure 10 Comparisons of experimental (solid line) and numerical (dotted line) waveforms for ultrasonic *P*-waves ((a)–(h)) and *S*-waves ((i)–(p)) at different effective pressures. Arrival times for both the numerical and experimental ultrasonic records are calculated and marked in the corresponding figures.

pressures. We see a general agreement between these two wavetrains in both amplitude and phase, even for waveforms particularly in the period of direct waves and in the initial portion of coda waves. The agreement for *P*-waveforms is much better than that of *S*-waveforms. Arrival times for both the numerical and experimental ultrasonic records are calculated and marked in the corresponding figures. We see that these arrival times agree well between numerical and experimental records, with the errors lower than 0.5%. Some discrepancies, however, are observed in waveforms for several effective pressures, possibly because of the imperfect poroelastic imaging of digital rocks in both mineral compositions and microstructures, the underestimation of poro-acoustoelastic constants at some effective pressures for elastic nonlinearity due to compliant pores, or the limitation of numerical methods in accuracy and absorbing boundary. Particularly, the laboratory experiment is carried out on a 3D cylindrical rock sample, whereas the presented numerical modeling is limited to 2D cases.

From Figure 10, we see that the amplitude of each wavetrain attenuates at almost the same level between the numerical and experimental records for all the effective pressures. Coda waves as a continuous wavetrain for the development of ultrasonic scattering waves exist in the tail

section of both the numerical and experimental records. The distribution and strength of coda waves exhibit strong apparent attenuation due to small-scale random heterogeneities as well as microstructures in the digital core. Since the sample presents moderate to weak scattering strength with respect to wavelengths, we estimate scattering attenuation by Sato (1977) the single scattering model (the simplest model to describe the coda). Compared to multiple scattering models, it is more suitable for cases where the lapse time measured from the origin time to the onset of the time window is much shorter than the mean free time in which waves propagate without scattering.

As shown in eq. (18), the acoustoelastic parameters with compliant pores are relevant to original microstructures. They are seldom influenced by effective pressures which only affect the effective elastic constants (D_{11}, D_{13}, D_{33}, D_{51}, D_{53}, and D_{55}). For isotropic pressure loading, only D_{11}, D_{33}, and D_{55} are affected, as shown in Figure 5a and 5b. The effect of effective pressures on the detail properties of waveform can be seen in Figure 10.

Following Guo et al. (2009), we calculate the coda quality factors Q_P and Q_S from the simulated amplitudes with time in the coda window by fitting the linear part of $\ln[A(f, t)]$ versus t, where $A(f, t)$ represents the observed root-mean-square (rms) amplitudes of the narrow bandpass-filtered waveforms with the centre frequency f. It is worth mentioning that the calculations of Q_P and Q_S assume no S-to-P conversion. For the S-wave excitation as pointed by Aki (1992), S-to-S scattering is more efficient than S-to-P scattering. As a result, the whole S coda mainly consists of scattered S waves with S-to-P scattering waves being neglected. Hence, the waveform motivated by a shear source can be approximated as the S coda. For the P-wave excitation, we only receive the displacement normal to the sample surface so that the tail portion of wavetrains can be regarded as the P-wave coda.

Figures 11 and 12 show the calculation procedures for P- and S-coda waves with the coda windows marked in the figures. As shown in Figure 4 from the experimental ultrasonic data, the stress-associated velocity variations demonstrate a distinct behavior in the low and high regimes of effective pressures, separated at P = 30 MPa. The corresponding experimental records between these two regimes of effective pressures show quite different features in both waveform and scattering attenuation. With the effective pressures greater/less than 30 MPa, we divide the simulated waveform data into two groups for best least-square fitting. According to Guo and Fu (2007) and Guo et al. (2009), the Q_s and Q_p can be obtained by P and S-wave coda. In addition, fluid flow in the saturated rocks will not influence the coda wave (Ma and Ba, 2020; Guo et al., 2018). Therefore, the values of Q_s and Q_p can be approximated as the scattering Q_s and Q_p.

From Figures 11 and 12, we estimate Q_P and Q_S at different effective pressures by the best least-square fitting to selected coda windows. The resulting Q_P and Q_S can be used to assess the stress-associated effect on scattering attenuation as well as on microstructures. Figure 13 compares the numerical and experimental Q_P^{-1} and Q_S^{-1} versus effective pressure. We see that the scattering attenuation due to small-scale heterogeneities seems sensitive to stress changes, presenting a strong nonlinear variation versus effective pressure. More importantly, we see an excellent agreement between the numerical and experimental results, implying the presented poro-acoustoelastic numerical modeling scheme for ultrasonic wave propagation in prestressed and fluid-saturated heterogeneous rocks can be reliably used to investigate the stress-associated scattering attenuation.

5. Discussions

The poro-acoustoelastic modeling with compliant pores for ultrasonic wave propagation in prestressed and heterogeneous fluid-saturated rocks, addressed in this article, involves with many issues. The most important problems should be stress-induced variations in both elastic modulus and scattering attenuation in laboratory environments. We will detail these aspects in this section.

The effect of effective pressures on the elastic wave velocity strongly depends on the stress-induced variation of static elastic moduli in porous rocks, which can be partitioned into background and local anomalous components. The former can be described by the traditional acoustoelastic theory for prestressed rocks without pores, whereas the latter becomes extremely complex because of the stress-induced deformation in microstructures and fluid-solid interactions under a large-magnitude stress loading. The Biot's dissipation by fluid-solid interactions under stress loading could be ignored for fluid-saturated rocks (Ba et al., 2013; Guo, 2008), whereas the microstructural deformation could be linear elastic, nonlinear elastic, and inelastic, depending on the loading magnitude and pore structures. In general, the conventional poro-acoustoelasticity theory accounts for linear elastic deformations (Winkler and Liu, 1996; Ba et al., 2013), possibly related to rock grains/stiff pores or limited to intermediate loading stresses for general pores, as demonstrated in Figure 4 for the effective pressures greater than 30 MPa. The nonlinear elastic deformation is usually subject to compliant pores (e.g., cracks, microfractures, grain joints, organic pores) under large loading stresses, as demonstrated in Figure 4 for the effective pressures less than 30 MPa. The stress-induced nonlinear deformation in compliant pores can be described by the dual-porosity model (Shapiro, 2003; David and Zimmerman, 2012), the Padé poro-acoustoelastic theory (Fu and Fu, 2017), and the poro-acoustoelastic theory with compliant pores for the second-order elastic constants

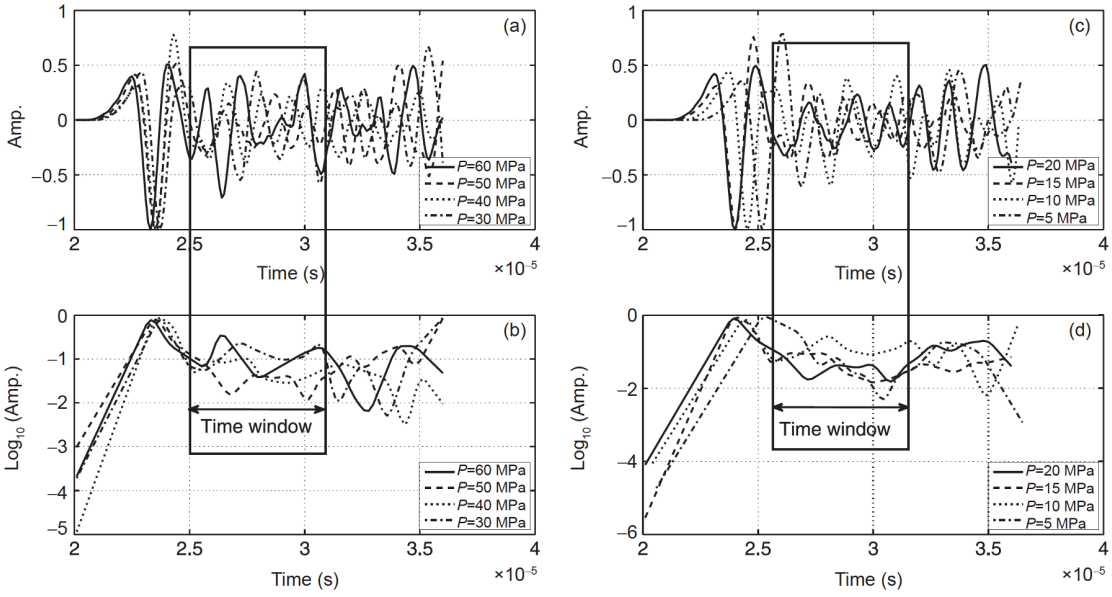

Figure 11 Calculation of coda quality factors Q_P for simulated *P*-coda waves at different effective stresses, with the coda windows marked in the figures. (a) & (b) Unfiltered *P*-waveforms and the corresponding envelope lines of logarithmic amplitudes for effective stresses from 30 to 60 MPa; (c) & (d) Unfiltered *P*-waveforms and the corresponding envelope lines (lower panel) of logarithmic amplitudes for effective stresses from 5 to 20 MPa.

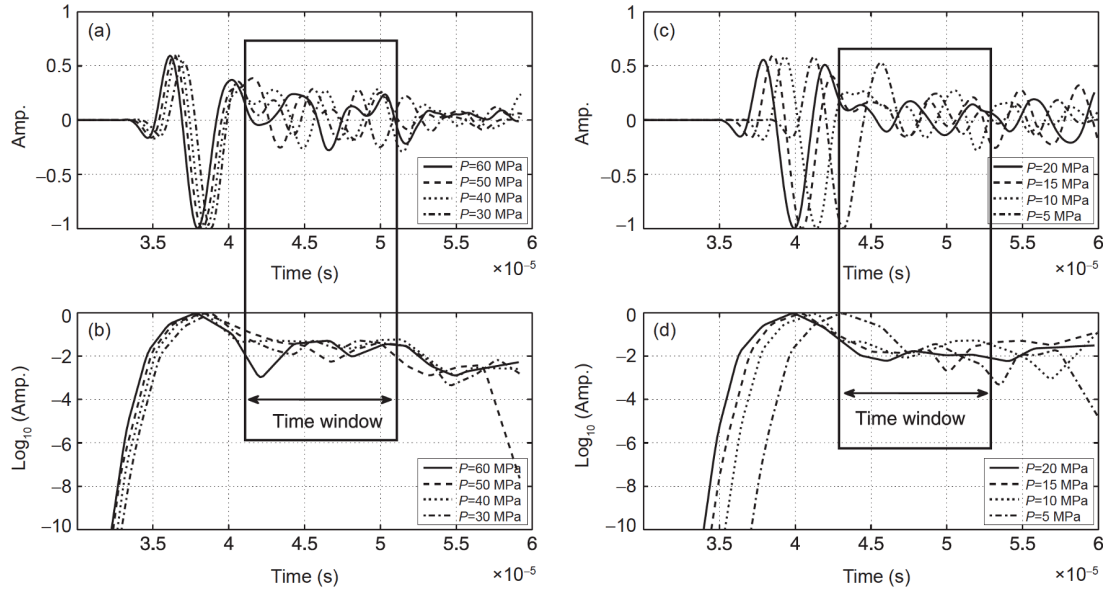

Figure 12 Calculation of coda quality factors Q_s for simulated *S*-coda waves at different effective stresses, with the coda windows marked in the figures. (a) & (b) Unfiltered *S*-waveforms and the corresponding envelope lines of logarithmic amplitudes for effective stresses from 30 to 60 MPa; (c) & (d) Unfiltered *S*-waveforms and the corresponding envelope lines of logarithmic amplitudes for effective stresses from 5 to 20 MPa.

(Fu and Fu, 2018) and the third-order elastic constants developed in this study (see Figure 5).

Based on the previous studies (Cheng and Toksöz, 1979; Zimmerman et al., 1986; Berryman and Pride, 1998; Kubair and Bhanu-Chandar, 2008; Cerit et al., 2009; David and Zimmerman, 2012), compliant mechanical defects, such as fracture surfaces, microcracks, and joint faces are all sensitive to stress. With decreasing aspect ratios, the strains of compliant pores increase with increasing pore pressures, intensifying the stress concentration and inducing the occurrence of an extensional process. In general, with increasing pore pressures under a stable confining pressure in saturated porous rocks, crack extension will increase the compliant-pore strains and decrease the rock stiffness. In general, the stress σ_c around a compliant pore could be related to the effective pressure P by

$$\sigma_c \propto LP, \tag{31}$$

where the stress concentration factor L, according to Kubair

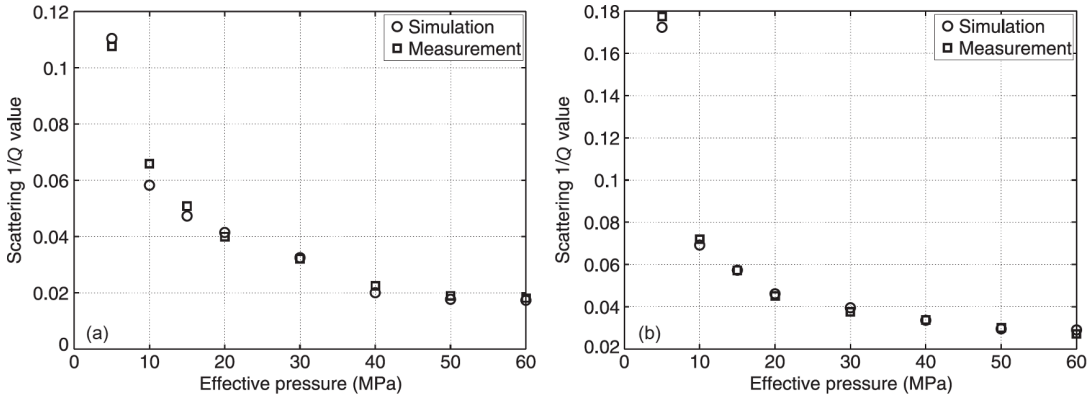

Figure 13 Comparisons of experimental (square) and numerical (circle) coda quality factors versus effective pressure for ultrasonic *P*-waves (a) and *S*-waves (b).

and Bhanu-Chandar (2008), can be expressed as functions of the quantities $\theta_{c(X)}$ (i.e., θ_{cL}, $\theta_{c\mu}$, θ_{cK}, θ_{cM5}, θ_{cM6}),

$$L \propto 1+\frac{1}{\gamma} \propto \left|\theta_{c(X)}\right|. \tag{32}$$

We see that the stress concentration factor increases with increasing quantities $\theta_{c(X)}$, significantly enhancing the stress σ_c around compliant pores possibly by hundreds of times higher than P. It implies that the work of loading stress could transform into dissipation induced by nonlinear deformation during the stress loading. The nonlinear elastic deformation of compliant pores tends to transform into inelastic deformation with further increasing loading stresses, as demonstrated by Sinha and Plona (2001) for plastic crack deformation attributed to sliding along crack surfaces. In this case, there are residual strains around compliant pores after stress disappearing, which has been manifested in experimental measurements by the misfit between loading and unloading variations in stress-induced velocity/attenuation (Guo et al., 2009). Figure 14 shows the stress-induced velocity variations versus pore pressure for ultrasonic *P*- and *S*-waves along the stress path under a constant confining pressure of 65 MPa with pore pressure increasing from 5 to 60 MPa at an increment of 5 MPa (loading procedure) and then returning to 5 MPa as fluid drains (unloading procedure). We see that the observed *P*- and *S*-wave velocities during unloading procedure (square) are less than those with loading procedure (circle). It implies a misfit crack opening and closure alternately during the cyclic loading and unloading procedures, with residual strains left around compliant pores after pore pressures unloading.

Scattering attenuation, as a result of changes in the physical state of material, is more sensitive to stress changes. The stress-induced scattering attenuation is mainly affected by boundary reflections, ultrasonic wavelengths, and stress-loading magnitudes. Stress-induced scattering attenuation from experimental ultrasonic records has been estimated using the single-scattering assumption (Guo et al., 2009), but may be controversial because of the potentially contaminated coda waves by boundary reflections from the side ends of sample. The effect of boundary reflections on ultrasonic coda waves in laboratory environments has been extensively addressed by numerical experiments (Fu et al., 2014; Zhang et al., 2014; Wei and Fu, 2014; Fu et al., 2016). In the current study, we employ a controllable PML absorbing boundary in numerical modeling to assure a consistent amplitude level of ultrasonic coda waves between the numerical and experimental results. That is, the equivalence of numerical and experimental boundary reflections implies that the coda waves might be contaminated to some degree by boundary reflections from the side ends of the sample. Based on the elaborate analyses (Fu et al., 2016) for the boundary reflections in laboratory environments, however, the emitted ultrasonic waves can be regarded approximately as a plane wave propagating mainly along the vertical direction, with few towards side directions. The side-direction waves are further attenuated by scattering in actual heterogeneous rocks, with fewer reaching the side ends to reflect. Furthermore, the rubber jackets around the sample can weaken boundary reflections to some degree. In contrast, the reverberations between the top and bottom surfaces are quite strong, which, however, are scattered by small-scale heterogeneities and reduced to less than 1/10 of the amplitude of direct wave in the time domain. In addition, the window length of coda waves can be selected to avoid the contamination of reverberations.

The *ka*-*kL* distribution of experimental measurements, as shown in Figure 8, demonstrates that the sample presents moderate to weak scattering strength with respect to wavelengths. From Figure 13, we see that scattering attenuation due to small-scale heterogeneities in the sample reduces with increasing effective pressures. Based on the previous studies (Kawahara and Yamashita, 1992), the scattering strength of small-scale heterogeneities depends strongly on *ka*. Figure 15 shows *ka* variations versus effective pressure in this study, indicating a consistent variation trend similar to that of coda

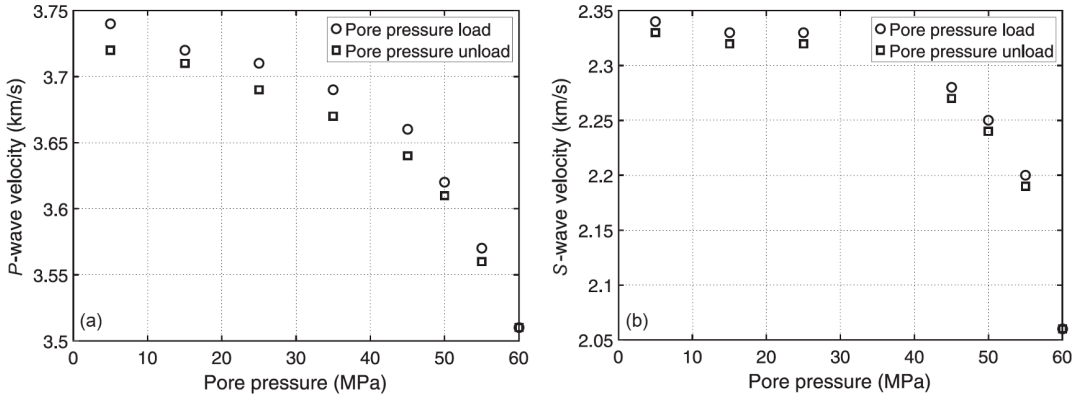

Figure 14 Stress-induced velocity variations versus pore pressure for ultrasonic *P*-waves (a) and *S*-waves (b) under a constant confining pressure of 65 MPa with pore pressure rising incrementally from 5 to 60 MPa (loading procedure) and then returning to 5 MPa (unloading procedure).

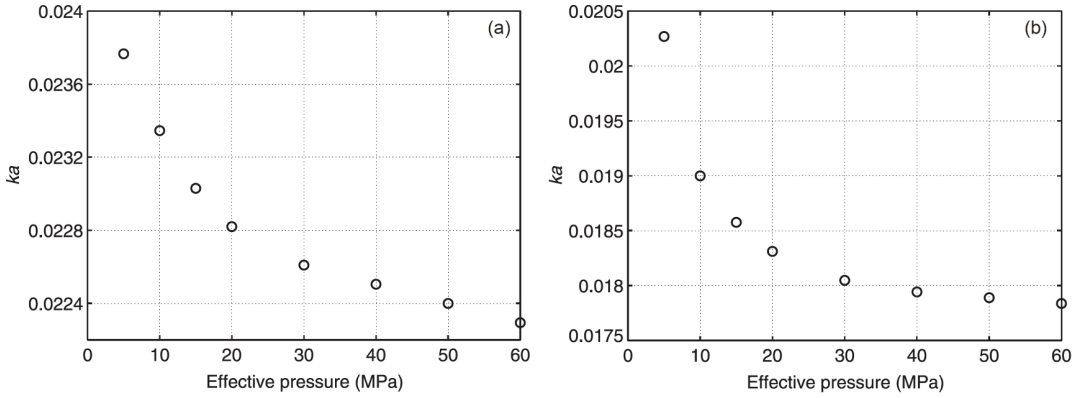

Figure 15 Variations of *ka* for ultrasonic *P*-waves (a) and *S*-waves (b) versus effective pressure in this study, indicating a consistent variation trend similar to that of coda quality factors shown in Figure 13.

quality factors shown in Figure 13. We see that with increasing effective pressures, compliant pores tend to be closed and scattering attenuation decreases nonlinearly. At this stage, increasing pore pressures tend to compress the pore linings of clays adjacent to framework grain contacts, increasing the stiffness for normal compression, decreasing the resistance to tangential displacements (Dvorkin et al., 1991), and consequently enhancing scattering attenuation. The resultant changes in compliant pores, in turn, affect the second- and third-order elastic constants. After the critical point occurring around 30 MPa, scattering attenuation reduces slowly to be stable with closed compliant pores.

We have noticed that in previous works, the stress-induced velocity variations in porous media are studied parallelly by poroelastic and poro-acoustoelastic methods, respectively. As indicated by Winkler and Liu (1996), the former approaches the stress-induced effect based upon closure of microcracks or compression of grain contacts, whereas the latter ignores microstructures and resorts to the third-order elastic constant. Comparing with poroelasticity, poro-acoustoelasticity can explain the physics of energy transformations through the elastic constant. The acoustoelastic deformation of porous rocks physically consists of two different types of energy transformations that are related to grains/stiff pores and compliant pores, respectively. The ideal prediction model should not only be able to express the elastic nonlinearity with physical meaning coefficients, but also explain the physics of the energy transformation of compliant-pore strains.

The poro-acoustoelastic theory with compliant pores could be by now the best choice for this issue based on the following three aspects. First, the conventional poro-acoustoelasticity approximates the strain energy function using third-order Taylor expansion by assuming small-amplitude strains. It accounts for the linear deformation of grains/stiff pores. For the model of Shapiro (2003) and David and Zimmerman (2012), the energy transformation induced by complaint-pore deformations is not considered. We improve the conventional theory by incorporating the dual-porosity model to account for nonlinear elastic deformations around compliant pores subject to high loading stresses. Secondly, the prediction model not only explains the energy transformation of compliant-pore strains, but also be able to express the elastic nonlinearity with physical meaning coefficients. Finally, the model only uses three parameters to provide better fitting of stress-induced variations in elastic moduli, whereas other

models involve more than three fitting parameters..

6. Conclusions

Elastic wave propagation and scattering in prestressed porous rocks can be approached by both poroelastic and poro-acoustoelastic methods. The former is often based on microstructural models and tends to make the problem extremely complex for real rocks with complicated pore structures. The latter, as a more general and model-independent description, is based on effective elastic constants by which to explain the physics of energy transformations of loading stresses. The acoustoelastic deformation of porous rocks could be linear elastic, nonlinear elastic, and inelastic, depending on the loading magnitude and pore structures. Linear elasticity is possibly related to grains/stiff pores or limited to intermediate loading stresses for general pores, whereas nonlinear elasticity is usually subject to compliant pores under large-magnitude loading stresses. Conventional poro-acoustoelasticity is based on the third-order elastic constant and accounts for linear elastic deformations. Modified poro-acoustoelasticity by incorporating the dual-porosity model can account for nonlinear elastic deformations around compliant pores subject to large-magnitude loading stresses. The nonlinear elasticity often leads to exponential changes in the experimentally observed elastic wave velocities.

By integrating theoretical analysis, experimental measurement, and numerical validation, we conduct a comprehensive study for elastic wave propagation and scattering in prestressed porous rocks. As an efficient alternative to experimental measurements, poro-acoustoelastic numerical simulations can provide a comprehensive investigation of the scaling dependence of velocity/attenuation on stresses and microstructures. We present a poro-acoustoelastic FE numerical modeling with compliant pores for ultrasonic wave propagation in prestressed and fluid-saturated heterogeneous digital rocks. We address in detail several key issues that challenge the comparison of numerical simulations and experimental measurements, such as digital imaging of heterogeneous poroelastic properties, estimation of acoustoelastic constants, numerical dispersion at high frequencies and strong heterogeneities, and contamination by boundary reflections. We conduct numerical simulations for a sandstone model from the experimental measurement with a fluid-saturated sandstone under a constant confining pressure of 65 MPa and increasing pore pressures from 5 to 60 MPa. The main conclusions can be summarized as follows:

(1) Experimental measurements with a fluid-saturated sandstone under different effective pressures demonstrate that the stress-induced velocity variations present a linear/nonlinear trend for the effective pressure greater/less than 30 MPa. The linear portion is possibly relevant to the deformation of grains/stiff pores and conforms to the prediction by conventional poro-acoustoelasticity, where compliant pores tend to be closed and their nonlinear effect could be neglected. For the nonlinear portion, the strong strain around compliant pores significantly decreases the stiffness of rocks, inducing an exponential drop in elastic wave velocities.

(2) We formulate a poro-acoustoelasticity with dual-porosity third-order elastic constants to describe the elastic nonlinearity of compliant pores. The prediction of elastic nonlinearity by the modified poro-acoustoelasticity shows a remarkable agreement with measurements, much better than the poro-acoustoelastic prediction with dual-porosity second-order elastic constants (Fu and Fu, 2018). Estimations of poro-acoustoelastic constants and microstructural coefficients are conducted carefully based on the experimental measurements.

(3) A typical digital rock workflow is used to create the digital imaging of the sandstone sample under study, which captures the composition and microstructure of sample. Identification of different minerals in in terms of their X-ray absorptivity demonstrates that the main mineral of sample is quartz, that is, the heterogeneity of sample depends on the size and distribution of quartz grains. We measure the heterogeneity of sample by extracting its autocorrelation length from digital cores with an attempt to obtain a rough estimation of scattering intensity. The resulting *ka*-*kL* distribution indicates that the sample presents a moderate scattering strength with respect to wavelengths.

(4) To guarantee the comparison of numerical and experimental waveforms for different loading stresses, poro-acoustoelastic numerical modeling of ultrasonic waves requires a high numerical accuracy to simulate subtle transmission/scattering effects across pores and grains in digital cores with minimal numerical dispersion. A modified finite-element method with triangular elements to mesh the digital poroelastic model is employed to discretize the modified poro-acoustoelastic equations. The second-order PML absorbing boundary is employed with alterable precision to estimate the amount of boundary reflections from the side ends of a sample core in the experimental environment.

(5) Numerical simulations demonstrate a general agreement with experimental wavetrains in both amplitude and phase for different effective pressures, particularly for waveforms in the period of direct waves and in the initial portion of coda waves. Comparisons of the scattering attenuation Q_P^{-1} and Q_S^{-1} at different effective pressures show an excellent agreement between numerical and experimental results, implying the presented numerical poro-acoustoelastic modeling scheme can be reliably used to investigate the stress-associated scattering attenuation.

(6) Numerical examples validate the applicability and

performance of poro-acoustoelastic FE modeling scheme to the stress-induced variations in both velocity and attenuation, which, in turn, could enable us to monitor changes in the subsurface *in-situ* stresses.

Acknowledgements *The authors would like to thank Laboratory of High-temperature and High-pressure Geodynamics, Chinese Academy of Sciences for great helps for preparing experimental data. This work was supported by National Natural Science Foundation of China (Grant No. 41821002), National Major Project of China (Grant No. 2017ZX05008007), and Strategic Priority Research Program of the Chinese Academy of Sciences (Grant No. XDA14010303).*

References

Aki K, Chouet B. 1975. Origin of coda waves: Source, attenuation, and scattering effects. J Geophys Res, 80: 3322–3342
Aki K. 1992. Scattering conversions P to S versus S to P. Bull Seismol Society Amer, 82: 1969–1972
Arns C H, Knackstedt M A, Pinczewski W V, Garboczi E J. 2002. Computation of linear elastic properties from microtomographic images: Methodology and agreement between theory and experiment. Geophysics, 67: 1396–1405
Arntsen B, Carcione J M. 2001. Numerical simulation of the Biot slow wave in water-saturated Nivelsteiner Sandstone. Geophysics, 66: 890–896
American Society for the Testing of Materials. 2002. Practice for Preparing Rock Core Specimens and Determining Dimensional Shape Tolerances. ASTM Standard 4543. American Society for the Testing of Materials, Philadelphia, PA
Ba J, Carcione J M, Cao H, Yao F, Du Q. 2013. Poro-acoustoelasticity of fluid-saturated rocks. Geophys Prospect, 61: 599–612
Berryman J G, Pride S R. 1998. Volume averaging, effective stress rules, and inversion for microstructural response of multicomponent porous media. Int J Solids Struct, 35: 4811–4843
Carcione J M. 2007. Wave Fields in Real Media: Wave Propagation in Anisotropic, Anelastic, Porous and Electromagnetic Media. 2nd ed. Elsevier
Carcione J M, Helle H B. 1999. Numerical solution of the poroviscoelastic wave equation on a staggered mesh. J Comput Phys, 154: 520–527
Carcione J M, Cavallini F. 2002. Poisson's ratio at high pore pressure. Geophys Prospect, 50: 97–106
Carcione J M, Helle H B, Pham N H. 2003a. White's model for wave propagation in partially saturated rocks: Comparison with poroelastic numerical experiments. Geophysics, 68: 1389–1398
Carcione J M, Helbig K, Helle H B. 2003b. Effects of pressure and saturating fluid on wave velocity and attenuation in anisotropic rocks. Int J Rock Mech Min Sci, 40: 389–403
Carcione J M, Picotti S. 2006. P-wave seismic attenuation by slow-wave diffusion: Effects of inhomogeneous rock properties. Geophysics, 71: O1–O8
Carcione J M, Quiroga-Goode G. 1995. Some aspects of the physics and numerical modeling of Biot compressional waves. J Comp Acous, 3: 261–280
Cerit M, Genel K, Eksi S. 2009. Numerical investigation on stress concentration of corrosion pit. Eng Failure Anal, 16: 2467–2472
Cheng C H, Toksöz M N. 1979. Inversion of seismic velocities for the pore aspect ratio spectrum of a rock. J Geophys Res, 84: 7533–7543
Dai N, Vafidis A, Kanasewich E R. 1995. Wave propagation in heterogeneous, porous media: A velocity-stress, finite-difference method. Geophysics, 60: 327–340
David E C, Zimmerman R W. 2012. Pore structure model for elastic wave velocities in fluid-saturated sandstones. J Geophys Res, 117: B07210
Deng J X, Zhou H, Wang H, Zhao J G, Wang S X. 2015. The influence of pore structure in reservoir sandstone on dispersion properties of elastic waves (in Chinese). Chin J Geophys, 58: 3389–3400
Dvorkin J, Derzhi N, Diaz E, Fang Q. 2011. Relevance of computational rock physics. Geophysics, 76: E141–E153
Dvorkin J, Derzhi N, Armbruster M, Fang Q, Wojcik Z. 2012. Method for determining rock physics relationships using computer tomographic images thereof. U.S. Patent No. 8,155,377. Washington D C: U.S. Patent and Trademark Office
Dvorkin J, Mavko G, Nur A. 1991. The effect of cementation on the elastic properties of granular material. Mech Mater, 12: 207–217
Franklin J A, Dusseault M B. 1989. Rock Engineering. New York: McGraw-Hill
Fu B Y, Fu L Y. 2017. Poro-acoustoelastic constants based on Padé approximation. J Acoust Soc Am, 142: 2890–2904
Fu B Y, Fu L Y. 2018. Poro-acoustoelasticity with compliant pores for fluid-saturated rocks. Geophysics, 83: WC1–WC14
Fu B Y, Fu L Y, Wei W, Zhang Y. 2016. Boundary-reflected waves and ultrasonic coda waves in rock physics experiments. Appl Geophys, 13: 667–682
Fu L Y, Zhang Y, Pei Z, Wei W, Zhang L. 2014. Poroelastic finite-difference modeling for ultrasonic waves in digital porous cores. Earthq Sci, 27: 285–299
Fukushima Y, Nishizawa O, Sato H, Ohtake M. 2003. Laboratory study on scattering characteristics of shear waves in rock samples. Bull Seismol Soc Am, 93: 253–263
Galvin R J, Gurevich B. 2007. Scattering of a longitudinal wave by a circular crack in a fluid-saturated porous medium. Int J Solids Struct, 44: 7389–7398
Galvin R J, Gurevich B. 2009. Effective properties of a poroelastic medium containing a distribution of aligned cracks. J Geophys Res, 114: B07305
Garboczi E J, Day A R. 1995. An algorithm for computing the effective linear elastic properties of heterogeneous materials: three-dimensional results for composites with equal phase Poisson ratios. J Mech Phys Solids, 43: 1349–1362
Gei D, Carcione J M. 2003. Acoustic properties of sediments saturated with gas hydrate, free gas and water. Geophys Prospect, 51: 141–158
Guo M. 2008. Response of seismic velocity and attenuation to stress changes in rocks (in Chinese). Doctoral Dissertation. Beijing: Institute of Geology and geophysics, Chinese Academy of Sciences
Guo M Q, Fu L Y. 2007. Stress associated coda attenuation from ultrasonic waveform measurements. Geophys Res Lett, 34: L09307
Guo M Q, Fu L Y, Ba J. 2009. Comparison of stress-associated coda attenuation and intrinsic attenuation from ultrasonic measurements. Geophys J Int, 178: 447–456
Guo J, Shuai D, Wei J, Ding P, Gurevich B. 2018. *P*-wave dispersion and attenuation due to scattering by aligned fluid saturated fractures with finite thickness: Theory and experiment. Geophys J Int, 215: 2114–2133
Gurevich B. 1996. On: "Wave Propagation in heterogeneous, porous media: A velocity-stress, finite difference method" by N. Dai, A. Vafidis, and E. R. Kanasewich (March-April 1995 GEOPHYSICS, p. 327–340). Geophysics, 61: 1230–1231
Gurevich B, Kelder O, Smeulders D M J. 1999. Validation of the slow compressional wave in porous media: Comparison of experiments and numerical simulations. Transp Porous Media, 36: 149–160
Gurevich B, Makarynska D, de Paula O B, Pervukhina M. 2010. A simple model for squirt-flow dispersion and attenuation in fluid-saturated granular rocks. Geophysics, 75: N109–N120
Guéguen Y, Sarout J. 2011. Characteristics of anisotropy and dispersion in cracked medium. Tectonophysics, 503: 165–172
Helle H B, Pham N H, Carcione J M. 2003. Velocity and attenuation in partially saturated rocks: Poroelastic numerical experiments. Geophys Prospect, 51: 551–566
Hu J, Fu L Y, Wei W, Zhang Y. 2018. Stress-associated intrinsic and scattering attenuation from laboratory ultrasonic measurements on shales. Pure Appl Geophys, 175: 929–962
Hu S Z, Fu L Y, Pei Z L. 2009. A boundary element method for the 2-D wave equation in fluid-saturated porous media (in Chinese). Chin J

Geophys, 52: 2364–2369
Hudson J A, Pointer T, Liu E. 2001. Effective-medium theories for fluid-saturated materials with aligned cracks. Geophys Prospect, 49: 509–522
Johnson P A, McCall K R. 1994. Observation and implications of nonlinear elastic wave response in rock. Geophys Res Lett, 21: 165–168
Johnson P A, Shankland T J. 1989. Nonlinear generation of elastic waves in granite and sandstone: Continuous wave and travel time observations. J Geophys Res, 94: 17729–17733
Kawahara J, Yamashita T. 1992. Scattering of elastic waves by a fracture zone containing randomly distributed cracks. Pure Appl Geophys, 139: 121–144
Kelder O, Smeulders D M J. 1997. Observation of the Biot slow wave in water-saturated Nivelsteiner sandstone. Geophysics, 62: 1794–1796
Kubair D V, Bhanu-Chandar B. 2008. Stress concentration factor due to a circular hole in functionally graded panels under uniaxial tension. Int J Mech Sci, 50: 732–742
Klimeš L. 2002. Correlation functions of random media. Pure Appl Geophys, 159: 1811–1831
Ma R, Ba J. 2020. Coda and intrinsic attenuations from ultrasonic measurements in tight siltstones. J Geophys Res Solid Earth, 125: e2019JB018825
Martin R, Komatitsch D, Ezziani A. 2008. An unsplit convolutional perfectly matched layer improved at grazing incidence for seismic wave propagation in poroelastic media. Geophysics, 73: T51–T61
Mason T G, Wilking J N, Meleson K, Chang C B, Graves S M. 2006. Nanoemulsions: Formation, structure, and physical properties. J Phys-Condens Matter, 18: R635–R666
Matsunami K. 1991. Laboratory tests of excitation and attenuation of coda waves using 2-D models of scattering media. Phys Earth Planet Inter, 67: 36–47
Mavko G, Mukerji T, Dvorkin J. 2009. The Rock Physics Handbook: Tools for Seismic Analysis of Oorous Media. Cambridge: Cambridge University Press. 113–164
Meegan Jr. G D, Johnson P A, Guyer R A, McCall K R. 1993. Observations of nonlinear elastic wave behavior in sandstone. J Acoust Soc Am, 94: 3387–3391
Meng W, Fu L Y. 2017. Seismic wavefield simulation by a modified finite element method with a perfectly matched layer absorbing boundary. J Geophys Eng, 14: 852–864
Nishizawa O, Satoh T, Lei X, Kuwahara Y. 1997. Laboratory studies of seismic wave propagation in inhomogeneous media using a laser Doppler vibrometer. Bull Seismol Soc Amer, 87: 809–823
Pervukhina M, Gurevich B, Dewhurst D N, Siggins A F. 2010. Applicability of velocity-Stress relationships based on the dual porosity concept to isotropic porous rocks. Geophys J Int, 181: 1473–1479
Picotti P, Aebersold R, Domon B. 2007. The implications of proteolytic background for shotgun proteomics. Mol Cell Proteomics, 6: 1589–1598
Pham N H, Carcione J M, Helle H B, Ursin B. 2002. Wave velocities and attenuation of shaley sandstones as a function of pore pressure and partial saturation. Geophys Prospecting, 50: 615–627
Pride S R, Berryman J G, Harris J M. 2004. Seismic attenuation due to wave-induced flow. J Geophys Res, 109: B01201
Roberts A P, Garboczi E J. 2000. Elastic properties of model porous ceramics. J Am Ceramic Soc, 83: 3041–3048
Saenger E H, Enzmann F, Keehm Y, Steeb H. 2011. Digital rock physics: Effect of fluid viscosity on effective elastic properties. J Appl Geophys, 74: 236–241
Saenger E H, Shapiro S A. 2002. Effective velocities in fractured media: A numerical study using the rotated staggered finite-difference grid. Geophys Prospect, 50: 183–194
Sato H. 1977. Energy propagation including scattering effects single isotropic scattering approximation. J Phys Earth, 25: 27–41
Sayers C M, Ebrom D A. 1997. Seismic traveltime analysis for azimuthally anisotropic media: Theory and experiment. Geophysics, 62: 1570–1582
Schoenberg M. 2002. Time-dependent anisotropy induced by pore pressure variation in fractured rock. J Seismic Explor, 11: 83–105
Shapiro S A. 2003. Elastic piezosensitivity of porous and fractured rocks. Geophysics, 68: 482–486
Shapiro S A, Kaselow A. 2005. Porosity and elastic anisotropy of rocks under tectonic stress and pore-pressure changes. Geophysics, 70: N27–N38
Sinha B K, Plona T J. 2001. Wave propagation in rocks with elastic-plastic deformations. Geophysics, 66: 772–785
Sivaji C, Nishizawa O, Kitagawa G, Fukushima Y. 2002. A physical-model study of the statistics of seismic waveform fluctuations in random heterogeneous media. Geophys J Int, 148: 575–595
Stacey G P, Gladwin M T. 1981. Rock mass characterisation by velocity and Q measurement with ultrasonics. Anelasticity Earth, 4: 78–82
Thomsen L. 1995. Elastic anisotropy due to aligned cracks in porous rock. Geophys Prospect, 43: 805–829
Toksöz M N, Johnston D H, Timur A. 1979. Attenuation of seismic waves in dry and saturated rocks: I. Laboratory measurements. Geophysics, 44: 681–690
Wang X, Zhang H, Wang D. 2003. Modelling seismic wave propagation in heterogeneous poroelastic media using a high-order staggered finite-difference method. Chin J Geophys, 46: 1206–1217
Wei W, Fu L Y. 2014. Monte carlo simulation of stress-associated scattering attenuation from laboratory ultrasonic measurements. Bull Seismol Soc Am, 104: 931–943
Wenzlau F, Müller T M. 2009. Finite-difference modeling of wave propagation and diffusion in poroelastic media. Geophysics, 74: T55–T66
Winkler K W, Liu X. 1996. Measurements of third-order elastic constants in rocks. J Acoust Soc Am, 100: 1392–1398
Winkler K W, McGowan L. 2004. Nonlinear acoustoelastic constants of dry and saturated rocks. J Geophys Res, 109: B10204
Wu R S. 1989. Seismic wave scattering. In: James D, ed. Encyclopedia of Solid Earth Geophysics. New York: Van Nostrand Reinhold. 1166–1187
Wu R S, Aki K. 1985. The fractal nature of the inhomogeneities in the lithosphere evidenced from seismic wave scattering. Pure Appl Geophys, 123: 805–818
Wu R S, Aki K. 1988. Multiple scattering and energy transfer of seismic waves—Separation of scattering effect from intrinsic attenuation II. Application of the theory to Hindu Kush region. Pure Appl Geophys, 128: 49–80
Zhang W H, Fu L Y, Zhang Y, Jin W J. 2016. Computation of elastic properties of 3D digital cores from the Longmaxi shale. Appl Geophys, 13: 364–374
Zhang Y, Fu L Y, Zhang L, Wei W, Guan X. 2014. Finite difference modeling of ultrasonic propagation (coda waves) in digital porous cores with un-split convolutional PML and rotated staggered grid. J Appl Geophys, 104: 75–89
Zhu X, McMechan G A. 1991. Numerical simulation of seismic responses of poroelastic reservoirs using Biot theory. Geophysics, 56: 328–339
Zimmerman R W, Somerton W H, King M S. 1986. Compressibility of porous rocks. J Geophys Res, 91: 12765–12777

(Responsible editor: Xingyao YIN)